True-to-scale DNA-density maps correlate with major accessibility differences between active and inactive chromatin

Márton Gelléri[1*+], Shih-Ya Chen[1*a], Aleksander Szczurek[1b], Barbara Hübner[2c] Michael Sterr[2d], Jan Neumann[1,3], Ole Kröger[4], Filip Sadlo[4], Jorg Imhoff[5], Yolanda Markaki[2e], Michael J. Hendzel[6], Marion Cremer[2], Thomas Cremer[2], Hilmar Strickfaden[1,6+], Christoph Cremer[1,3,4,7+]

1.) Institute of Molecular Biology (IMB), Mainz, Germany

2.) Biocenter, Dept Biology II, Ludwig Maximilian University (LMU), Munich, Germany)

3.) Max Planck Institute for Chemistry, Mainz, Germany

4.) Interdisciplinary Center for Scientific Computing (IWR), University Heidelberg, Heidelberg, Germany

5.) Neuroconsult GmbH, Heidelberg, Germany

6.) Department of Oncology, Cross Cancer Institute, University of Alberta, Edmonton, Alberta, Canada

7.) Kirchhoff Institute of Physics, University Heidelberg, Heidelberg, Germany

*equal contributions

[a]SC, present address: Zeiss Innovation Hub Dresden, Germany
[b]AS, present address: Department of Biochemistry, Oxford University, Oxford, UK
[c]BH, present address: Nanyang Technological University, School of Biological Sciences & NTU Institute of Structural Biology (NISB), Singapore
[d]MS, present address: Helmholtz Center Munich, Institute of Diabetes and Regeneration Research (IDR), Neuherberg, Germany
[e]YM, present address: Department of Biological Chemistry, David Geffen School of Medicine, University of California, Los Angeles, CA 90095, USA

+corresponding authors:
Christoph Cremer: C.Cremer@imb-mainz.de
Márton Gelléri: M.Gelleri@imb-mainz.de
Hilmar Strickfaden: hilmar@ualberta.ca; hilmar@structural-epigenetics.org

Keywords: active and inactive nuclear compartments (ANC and INC), true-to-scale DNA density maps (Mbp/µm^3), microinjected nanobeads, replication domains (RDs), single molecule localization microscopy (SMLM), structured illumination microscopy (SIM), electron spectroscopic imaging (ESI), quantitative image analysis, Voronoi-tessellation

Summary

Chromatin compaction differences may have a strong impact on accessibility of individual macromolecules and macromolecular assemblies to their DNA target sites. Estimates based on fluorescence microscopy with conventional resolution, however, suggested only modest compaction differences (~2-10x) between active and inactive nuclear compartments (ANC and INC). Here, we present maps of nuclear landscapes with true-to-scale DNA-densities, ranging from <5 Mbp/µm^3 to >300 Mbp/µm^3. Maps were generated from individual human and mouse cell nuclei with single-molecule localization microscopy at ~20 nm lateral and ~100 nm axial resolution and supplemented by electron spectroscopic imaging. Microinjection of fluorescent nanobeads with sizes corresponding to macromolecular assemblies for transcription and replication into nuclei of living cells, demonstrated their localization and movements within the ANC and exclusion from the INC.

Introduction

Understanding the functional behavior of genomes requires knowledge of the dynamic biochemical and physical chromatin loop organization (Gasser and Laemmli, 1987; Neguembor et al., 2021) and its consequences for the accessibility of individual macromolecules, condensates with proteins and RNAs, as well as of structured macromolecular assemblies involved in nuclear functions. Microscopic studies of nuclear architecture have provided evidence for a multitude of chromatin ensembles with chromatin domains (CDs), chromosome territories (CTs), as well as active and inactive nuclear compartments (Cremer et al., 2020a; Cremer et al., 2015; Maslova and Krasikova, 2021; Nguyen et al., 2020; Nir et al., 2018; Strickfaden, 2021). Chromatin ensembles, such as topologically associating domains (TADs) and A- and B-compartments, were independently identified by genome wide measurements of 3D

68 chromatin contacts (Dekker et al., 2017; Di Stefano et al., 2016; Kempfer and Pombo,
69 2020; Moretti et al., 2020) (for a glossary of currently used nomenclatures and
70 conceptual differences, see supplemental information in (Cremer et al., 2020b).
71 Physical maps of nuclear landscapes, supplemented with biochemical information
72 about epigenetic markers and attachment sites of specific macromolecules and
73 functional complexes, have revolutionized our views on nuclear organization. How
74 nuclear compartments are established and maintained, and how they interact
75 functionally, has remained a largely unsolved problem (Belmont, 2021; Misteli, 2020).
76 Higher order chromatin arrangements differ substantially not only between different
77 cell types and species, but also from cell to cell of a given cell population of the same
78 cell type (Cardozo Gizzi, 2021; Strickfaden, 2021). This variability may reflect
79 stochastic features of 4D spatial genomics (Finn and Misteli, 2019), while other
80 features, including the space-time organization of nuclear landscapes at mesoscale,
81 reflect a functionally important preciseness of genome organization (see Discussion).
82 In this study, we deal with the still unresolved problem of true-to-scale
83 compaction levels (in terms of Mbp/μm^3) of chromatin ensembles, constituting active
84 and inactive nuclear compartments. These were previously identified by topological
85 linking of relative chromatin density maps with functionally relevant nuclear hallmarks
86 (Cremer et al., 2020a; Cremer et al., 2015) or by 3D-DNA contact frequency data
87 (Lieberman-Aiden et al., 2009). At face value, a large body of evidence obtained in
88 previous studies suggests only modest compaction and accessibility differences for
89 functional macromolecules and macromolecular aggregates between active and
90 inactive chromatin ensembles. Our present study challenges this concept.
91 Figure 1a-b shows views of higher order chromatin organization based on
92 apparently ‘open’ chromatin loop configurations. Accordingly, an interchromatin space
93 expanding both within the interior and outside of individual loops seems wide enough

to allow penetration of individual macromolecules and complete macromolecular machineries (Figure 1c). In contrast, concepts of a much more 'crumpled' organization of chromatin (Figure 1d), and a 'closed' configuration of densely packaged nucleosomes (Figure 1e), may constrain the penetration of individual macromolecules into the interior of chromatin ensembles, and exclude the penetration of macromolecular machineries or phase-separated condensates (Maeshima et al., 2015). Our current version of the ANC-INC model (Figure 1f) supports this concept (Cremer et al., 2020a) (see below).

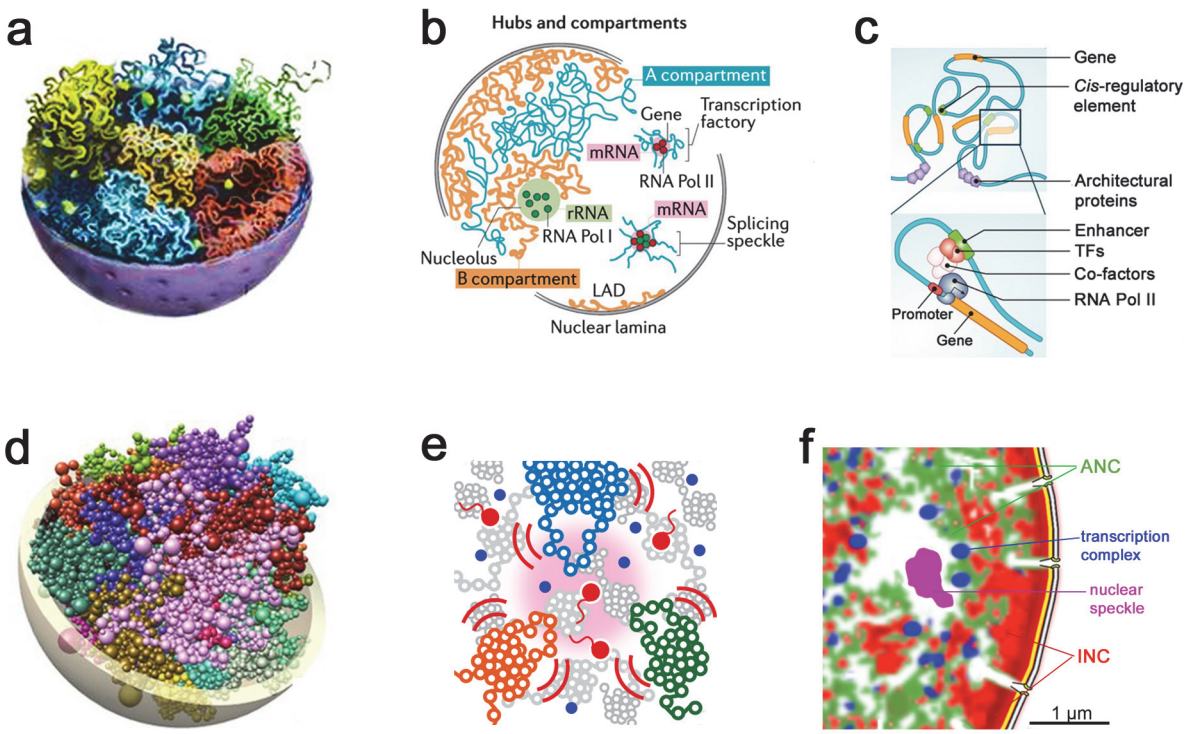

Figure 1: Views of 3D nuclear landscape
Current views of nuclear organization at mesoscale agree that chromosomes occupy distinct territories (CTs)/domains (Cremer and Cremer, 2010; Cremer et al., 2015; Dekker et al., 2017; Di Stefano et al., 2016; Kempfer and Pombo, 2020; Moretti et al., 2020; Paulsen et al., 2018). Current concepts of chromatin compaction, however, range from relatively open chromatin loop configurations ***a*** *(Dekker et al., 2017);* ***b*** *(Kempfer and Pombo, 2020);* ***c*** *(Moretti et al., 2020) to proposals as in* ***d*** *describing the crumpled organization of chromatin as little balls without giving an opinion on the density of chromatin inside (Paulsen et al., 2018).* ***e*** *Higher order chromatin organization of chromatin based on nucleosome clusters (NCs)(Babokhov et al., 2020). Red dots: RNAPII; blue dots: transcription factors. NCs may form the first level of higher order chromatin structures beyond individual nucleosomes (Ricci et al., 2015).* ***f*** *ANC-INC model of nuclear architecture (Cremer et al., 2020a; Cremer et al., 2015). The active nuclear compartment (ANC) comprises the Interchromatin compartment (IC). IC-channels start at nuclear pores. The IC forms a network throughout the nuclear interior and expands at certain*

sites into wider IC-lacunae, which carry splicing speckles and other nuclear bodies. It is lined by the perichromatin region (PR) with less dense and more accessible chromatin (green). The inactive nuclear compartment (INC) carries more compact and poorly accessible chromatin (red); for further details see Figure 6 and text.

It is of note that many published cartoons show details of nuclear landscapes that are not drawn to scale. True-to-scale maps of spatial chromatin compaction, however, is a fundamental issue of chromatin accessibility and inaccessibility with major functional implications (see Discussion). For a comprehensive solution of this issue, super-resolved maps across entire nuclear landscapes are required, providing absolute local DNA densities (Mbp/μm^3) instead of relative density differences (Schmid et al., 2017). Studies performed with the resolution limit of conventional fluorescence microscopy (~200 nm in the object plane, and ~600 nm along the optical axis), have suggested relatively small density differences between euchromatin and heterochromatin regions (Gorisch et al., 2003; Lenart et al., 2003; Verschure et al., 2003). Insufficient resolution, however, underestimates the true density related differences between euchromatic and heterochromatic regions, comparable to a landscape of a mountain region, recorded from an airplane with a poor resolution camera, that levels the differences between high mountains and deep valleys. Estimates of absolute nucleosome densities in live HeLa cell nuclei, obtained by a combination of Fluorescence Correlation Spectroscopy and Confocal Imaging (Weidemann et al., 2003), revealed about tenfold intranuclear differences in local nucleosome density, ranging from about 25 μM to 250 μM. Assuming 200 bp per nucleosome (including linker DNA), these values amount to about 3 Mbp/μm^3 for low density regions and 30 Mbp/μm^3 for high density regions. The authors mentioned that they could not exclude the possibility of the formation of local barriers only detectable with a much higher structural resolution. Studies of nuclei in live-murine cells performed with laser confocal microscopy (Imai et al., 2017) suggested a moderate

145 accessibility barrier of non-nucleosomal materials (proteins/RNAs) that constrains the
146 diffusion of proteins into heterochromatin.

147 Whereas studies with conventional optical resolution comprises an observation
148 volume in the order of ~10,000 nucleosomes (Weidemann et al., 2003), the improved
149 structural resolution obtained with single molecule localization microscopy (SMLM) (for
150 reviews see (Cremer and Masters, 2013; Gould and Bewersdorf, 2012; Khater et al.,
151 2020; Lelek et al., 2021; Schermelleh et al., 2019) allows the visualization of individual
152 clusters with less than 100 nucleosomes. Previous microscopic studies performed at
153 this highly enhanced resolution level have indicated dense assemblies of nucleosomes
154 in heterogeneous groups comprising a few kb of DNA, termed nucleosome clutches
155 (NCs) (Ricci et al., 2015). NCs provide candidate structures that may represent
156 building blocks for all higher-order nucleosome structures above the single
157 nucleosome level, such as chromatin domains or TAD-like structures (Bintu et al.,
158 2018; Ricci et al., 2015; Szabo et al., 2019; Szabo et al., 2018).

159 The present quantitative, high-resolution study presents the first true-to-scale
160 3D DNA density maps of the absolute heights of DNA density peaks and valleys across
161 entire nuclear landscapes of individual cells in terms of Mbp/μm^3 at nanometer-scale
162 resolution. Differences between high density chromatin structures assigned to the INC
163 and low DNA density regions assigned to the ANC (Babokhov et al., 2020; Cremer et
164 al., 2020a) range from <5 Mbp/μm^3 to >300 Mbp/μm^3 and are much larger than DNA
165 compaction differences claimed in previous studies with conventional microscopic
166 resolution. In addition, we performed microinjection experiments with 20 and 40 nm
167 sized fluorescent nanobeads, reflecting sizes of macromolecular assemblies for
168 transcription and replication (Maeshima et al., 2015), and demonstrate their
169 preferential enrichment in the active nuclear compartment (ANC) and exclusion from
170 the inactive compartment (INC). These findings support a substantially lower

171 compaction in the ANC associated with a higher accessibility of chromatin ensembles
172 compared to the INC, with major implications for the functional organization of the cell
173 nucleus.
174
175 **Results**

176 **Determination of absolute DNA densities across nuclear landscapes**

177 Single Molecule Localization Microscopy (SMLM) (Cremer et al., 2017)
178 combined with fluctuation assisted Binding Activated Localization Microscopy (fBALM)
179 (Szczurek et al., 2018; Szczurek et al., 2017) was used to record millions of blinking
180 events of the fluorophore Sytox Orange, bound to double-stranded DNA in single light
181 optical nuclear sections from morphologically intact human and mouse fibroblasts and
182 from HeLa, as an example of a human cancer cell-line. Since Syto Nucleic Acid Stains
183 (ThermoFisher Scientific) bind to both DNA and RNA, RNA was removed by treatment
184 with an RNase cocktail before staining with Sytox Orange. In line with our major goal
185 to determine absolute DNA densities of euchromatic and heterochromatic regions at
186 high resolution, Sytox orange shows a more equal affinity to both GC and AT rich DNA,
187 compared to DAPI and Hoechst 33342, which bind preferentially to AT rich DNA
188 (Chazotte, 2011) (Supplemental Figure S1).

189 Figure 2 presents the color-coded, Voronoi-tessellated true-to-scale 3D DNA
190 density SMLM-fBALM image obtained from a mid-plane optical section through a
191 human fibroblast nucleus (BJ1) (Figure 2a) in G1 stage (Supplemental Figure S2). The
192 image was generated from ~1.5 million spatially mapped blinking events, registered in
193 50,000 consecutively recorded frames (Supplemental Figure S3). Single Molecule
194 Positions (SMPs) of these events were located within an optical section of about 100
195 nm thickness with an average localization precision of ~50 nm along the optical axis
196 and an average lateral localization precision of ca. 8 nm (for details of this procedure

197 see Methods). Figures 2b, c (upper panels) show selected regions with increasing
198 magnifications. For panels a-c, a color-coded scale bar for 3D DNA densities with
199 emphasis on the range >5 Mbp/μm^3 and <40 Mbp/μm^3 is presented at the top of Figure
200 2b. Figure 2c (lower panel) presents the Voronoi tessellations used for reconstructions
201 of images 2c (upper panel). Figure 2d presents the same panel shown in Figure 2c
202 with another color-bar code (below) that emphasizes the range of 3D DNA densities
203 from >40 Mbp/μm^3 up to ~350 Mbp/μm^3.

204 Absolute DNA densities (Mbp/μm^3) were calculated as follows: In addition to the
205 total number of SMPs, we estimated both the volume, comprising about 1/20th of the
206 nuclear volume, and the total DNA content of the 100 nm thick optical section. From
207 these numbers, we calculated that a single SMP in this BJ1 nucleus was representative
208 on average for about 200 bp, that is roughly the DNA surrounding a single nucleosome
209 (see Methods for further details). Next, we used 2D Voronoi-tessellation (Andronov et
210 al., 2016; Levet et al., 2015) for partitioning 2D SMP density images into 2D polygonal
211 images. Assuming that each 2D polygon represents in fact a 3D polygonal prism with
212 a depth of 100 nm, we calculated the average DNA density for each prism by dividing
213 its DNA content (based on the number of SMPs) by its volume. Polygonal Voronoi
214 prisms were color-coded corresponding to 3D DNA density estimates, ranging from <5
215 Mbp/μm^3 (white) to >40 Mbp/μm^3 (deep red), respectively, as indicated in the color-
216 coded scale for 2a-c. A further unfolding of color codes for densities >40 Mbp/μm^3 up
217 to ~350 Mbp/μm^3 and corresponding SMP densities is provided in the color scale
218 column in Figure 2d.

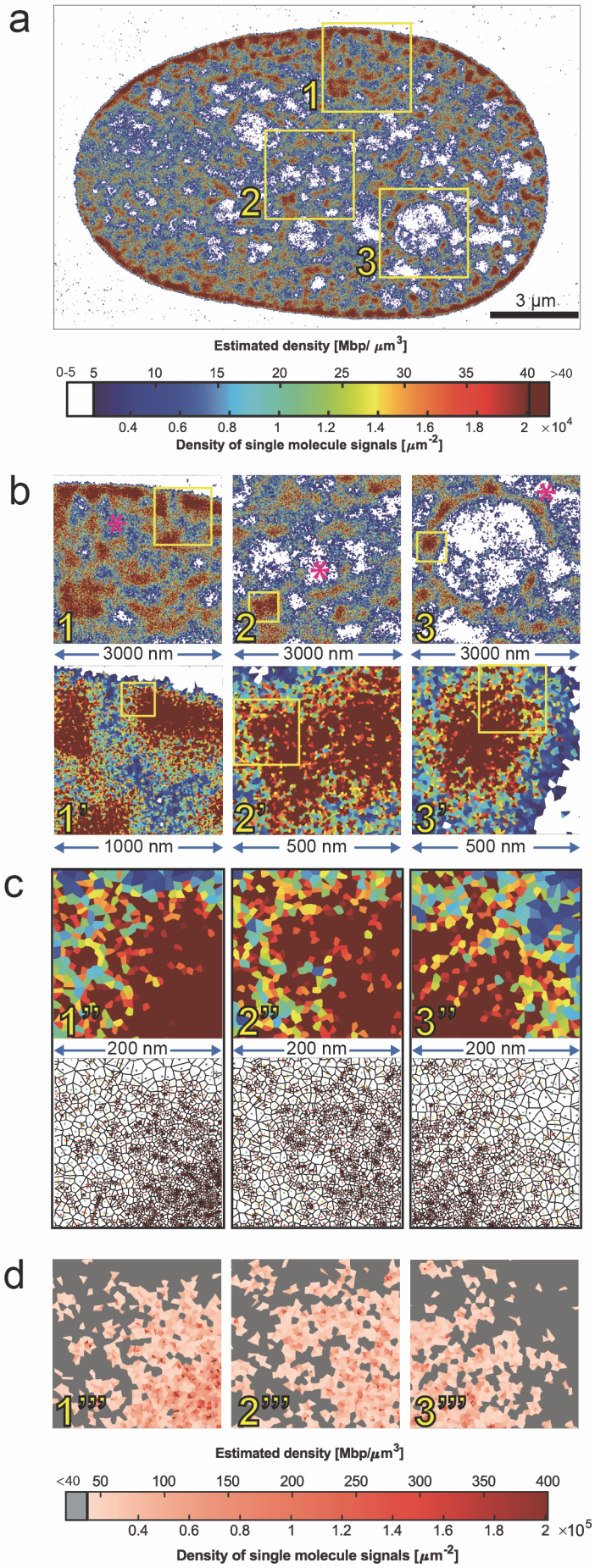
a
1
2
3
3 µm
Estimated density [Mbp/ µm3]
0-5 5 10 15 20 25 30 35 40 >40
0.4 0.6 0.8 1 1.2 1.4 1.6 1.8 2 ×10^4
Density of single molecule signals [µm-2]
b
1
2
3
3000 nm
3000 nm
3000 nm
1'
2'
3'
1000 nm
500 nm
500 nm
c
1''
2''
3''
200 nm
200 nm
200 nm
d
1'''
2'''
3'''
Estimated density [Mbp/µm3]
<40 50 100 150 200 250 300 350 400
0.4 0.6 0.8 1 1.2 1.4 1.6 1.8 2 ×10^5
Density of single molecule signals [µm-2]

219

Figure 2: High-resolution, true-to-scale DNA density landscape of a human fibroblast nucleus

a *Voronoi-tessellated SMLM-fBALM image of a mid-optical section (thickness ~100 nm through a diploid human fibroblast cell nucleus (BJ1) stained with Sytox Orange (see Methods for further explanation how this image was generated). The color code indicates the estimated range of 3D DNA densities from <5 Mbp/µm^3 to >40 Mbp/µm^3, reflecting 2D SMP densities <2,500 SMPs/µm^2 to >20,000 SMPs/µm^2 (see Supplemental Figure S3, Supplemental Videos S1a,b) and Results for 3D DNA densities estimated from 2D SMP densities in 100 nm thick sections).* ***b, 1-3*** *Magnifications of the three boxed areas in (a) demonstrate sites located at the nuclear periphery (1) and in the nuclear interior (2, 3); edge length 3000 nm. Asterisks denote IC-lacunae.* ***b, 1'–3'*** *Further magnification of boxed areas in (1-3), edge lengths 1000 nm (1'), and 500 nm (2',3').* ***c, 1''–3''*** *upper row: Further magnification of boxed areas in (1'-3'), edge length 200 nm. lower row: Individual Voronoi centers (seeds) are shown for the same Voronoi areas as in 1'' – 3''.* ***d, 1'''–3'''*** *same areas as in c 1'' depicted here with another color code (shown at bottom) for 3D DNA densities from 40 Mbp/µm^3 to about 350 Mbp/µm^3, reflecting a range of 2D SMP densities between ~20,000 and ~180,000 SMPs/µm^2.*

Figure 3 exemplifies a mid-optical section of a nucleus from the near triploid human cancer cell line HeLa. Based on its small size, we assume that this nucleus also represents a G1 stage (Cremer et al., 2003). This color-coded, Voronoi-tessellated SMLM-fBALM image was constructed from about 1.2 million SMPs of DNA-bound, blinking Sytox Orange molecules registered in 50,000 consecutive frames within a 100 nm thick optical section. True-to-scale DNA densities were estimated as described above. Note that estimates of absolute DNA densities estimates are conservative and would increase by a factor 2 in case of a G2 DNA content. Towards the nuclear periphery, we note high-density chromatin ensembles with diameters up to several hundred nm, surrounded by chromatin with low DNA densities. Supplemental Figure S4 presents the SMLM-fBALM image of the mid-optical section from another HeLa cell nucleus, which shows the typical structural features of the ANC-INC model, but differs substantially from the example shown in Figure 3 with regard to a more expanded ANC at the cost of a reduced INC. Arguably, this nuclear landscape may reflect a more advanced interphase stage (Nagano et al., 2017). A detailed study of different interphase stages, however, was beyond the scope of our present study.

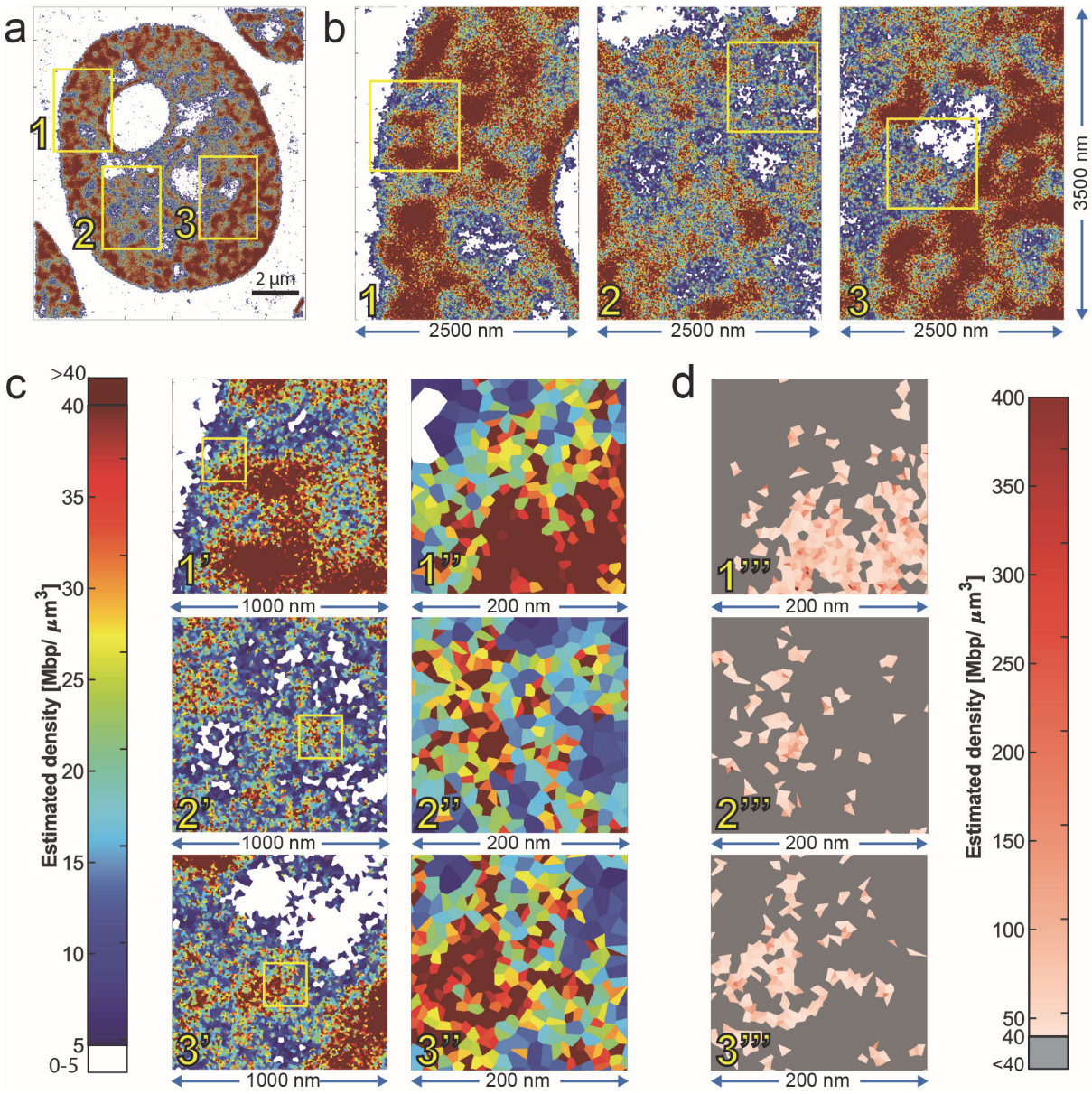

Figure 3: High-resolution, true-to-scale DNA density landscape of a HeLa cell nucleus

a *SMLM-fBALM image (Voronoi-tessellation) of a mid-optical section (thickness ~100 nm) through a HeLa cell nucleus.* ***b, 1-3*** *Magnifications of the three boxed areas in (a); edge lengths 2.5 µm x 3.5 µm.* ***c*** *color code shown on the left presents estimates of absolute densities for 0-5 Mbp/µm³ (white), and the range from 5 to (dark blue) to >40 Mbp/µm³ (dark red) (as described in Figure 2).* ***c, 1'-3'*** *Further magnification of boxed areas in (b,1-3); edge length 1000 nm;* ***c, 1''-3''*** *Further magnification of boxed areas in c,1'- 3'; edge length 200 nm, depicts individual color-coded Voronoi cells and clusters with the same color.* ***d, 1'''- 3'''*** *presents the same regions as in c 1''- 3'' shown in another color code (also described in Figure 2) to demonstrate the range of apparent DNA densities from 40 Mbp/µm³ (light red) up to maximum densities of 400 Mbp/µm³ (dark red).*

In summary, Figures 2 and 3 exemplify the potential of our approach to identify the widely different, true-to-scale 3D DNA densities of chromatin ensembles and their

nuclear arrangements across entire nuclear landscapes at mesoscale and nanoscale structural resolution.

Figure 4 shows a comparison of the DNA landscapes of a mouse C3H 10T1/2 fibroblast nucleus obtained from a Voronoi-tessellated SMLM-fBALM image (Figure 4a) and from electron spectroscopic imaging (ESI) (Hendzel and Bazett-Jones, 1996) (Figure 4b-e) with the same thickness (100 nm) of light optical and physical ultra-thin midsections, respectively. The two mouse fibroblast nuclei vary with regard to the more expanded IC (blue) in the nucleus studied with ESI; apart from this their DNA-density landscapes appear remarkably similar with less dense chromatin in the PR. In both human and mouse nuclei we note an enrichment of highly compact DNA at the nuclear periphery. In contrast to the human fibroblast nucleus, the mouse fibroblast nucleus carries prominent clusters of constitutive heterochromatin, called chromocenters (depicted by arrows).

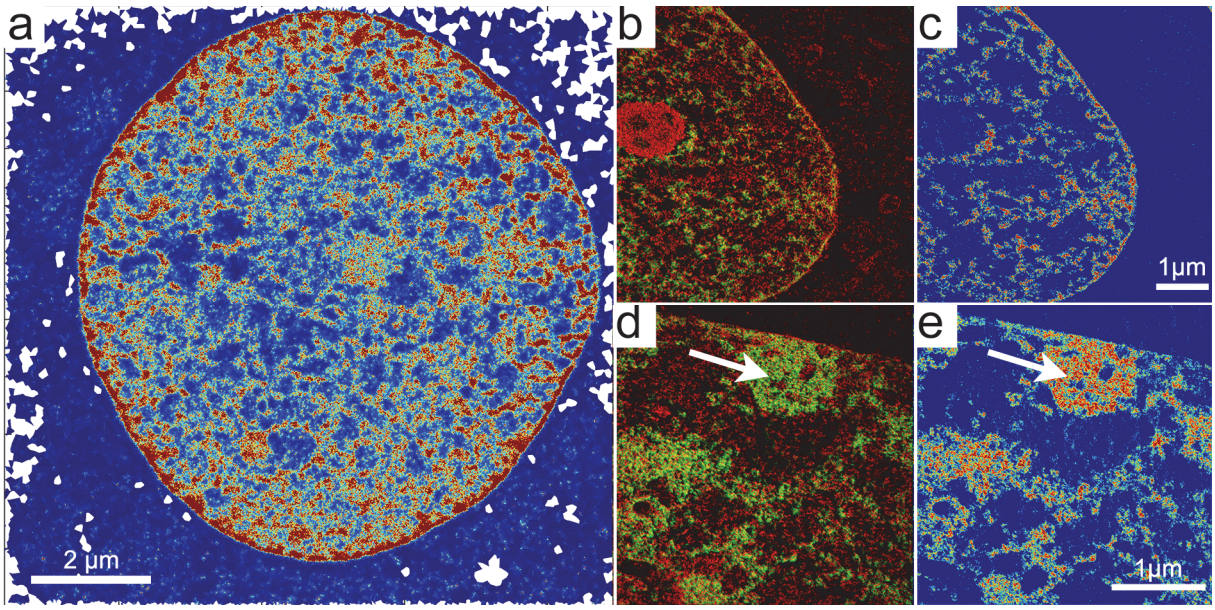

Figure 4: Comparison of high-resolution DNA landscapes of mouse C3H T1/2 fibroblast nuclei recorded with SMLM and ESI

a *100 nm optical mid-section through a mouse C3H T1/2 fibroblast nucleus recorded with SMLM-fBALM.* ***b-e*** *ESI micrographs taken from acrylic 100 nm thin mid-sections through another C3H T1/2 fibroblast nucleus.* ***b*** *and* ***d*** *show superimposed elemental maps of phosphorus (green) and nitrogen (red).* ***c*** *and* ***e*** *present the phosphorus map only, color-coded for different phosphorus densities as a reflection of DNA densities. For better comparison, the same color-coded look-up table (jet) was used for SMLM (a) and ESI images (c,e; blue indicates lowest DNA densities that belong to the IC, lined by light blue and green colored*

292 *intermediate densities (PR); red marks high DNA compaction attributed to the INC (compare*
293 *Figures 2 and 3). Arrows in (d) and (e) indicate examples of chromocenters. In order to secure*
294 *that only the DNA landscape was recorded, RNA was digested in both nuclei prior to imaging.*
295

296 **Localization and constrained movements of microinjected nanobeads within the**
297 **ANC**

298 Evidence presented above supports DNA density differences, ranging from
299 <5 Mbp/μm^3 in the ANC to >300 Mbp/μm^3 in the INC. For a rough idea of a sterical
300 accessibility barriers imposed by chromatin, we estimated 3D distances between the
301 surfaces of nucleosomes, represented by 10 nm sized spheres uniformly arranged in
302 3D space in comparison to a spherical protein with 5 nm diameter, and a 20 nm sized
303 condensate or macromolecular machinery. We assumed DNA fully packaged with
304 nucleosomes at different DNA densities of 5, 30, 60 and 150 Mbp/μm^3 (Figure 5a). At
305 face value, this scheme favors the hypothesis of an accessibility barrier of dense
306 nucleosome aggregates attributed to the INC. Apparently, there is little room left for
307 different geometrical arrangements of nucleosome spheres at very high DNA densities.
308 On the contrary, geometrical nucleosome arrangements at low densities (<5 Mbp/μm^3)
309 provide sufficient nucleosome free space for a variety of individual loop structures,
310 which allow a high degree of accessibility for macromolecules and macromolecular
311 complexes/condensates. Since the space-time dynamics of chromatin domains in
312 nuclei of living cells is currently not well understood (see Discussion), it is not possible
313 to conclude from the observed DNA density differences in fixed cell nuclei, to which
314 extent chromatin in the INC with high compaction levels may constrain the accessibility
315 of individual proteins and RNAs or fully exclude macromolecular machineries and
316 condensates, assembled within the ANC. For an experimental test, we microinjected
317 fluorescent beads with 20 nm and 40 nm diameter, respectively, into nuclei of living
318 HeLa cells (Figure 5b-e) and of C3H 10T1/2 cells (Figure 5f-i). The sizes of these

319 nanobeads were chosen to approximate sizes of transcription- and replication-
320 machineries or phase-separated droplets. HeLa cells used for microinjection
321 experiments were either kept in isotonic (290 mOsm) medium (Figure 5b), or in
322 hypertonic (570 mOsm) medium (Figure 5c), resulting in the rapid induction (~1 min)
323 of hyper-condensed chromatin (HCC). When cells with HCC were re-incubated in
324 medium with physiological osmolarity (290 mOsm), nuclei with normally condensed
325 chromatin (NNC) were quickly restored, even after several NNC-HCC-NCC cycles
326 (Albiez et al., 2006). For both states of chromatin compaction, analysis of nanobead
327 positions in fixed cell nuclei demonstrated their presence in less condensed chromatin
328 attributed to the ANC (Figure 5d, e). Corresponding DNA (DAPI) intensity profiles are
329 shown by line scans through nuclei encompassing the site of a nanobead
330 (Supplemental Figures S5 and S6). Most HeLa nuclei with nanobeads, including cells
331 after a NCC-HCC-NCC cycle, were able to pass through mitosis and formed two
332 daughter cells with apparently normal nuclei. Notably, live cell imaging demonstrated
333 mitotic cells with nanobeads excluded from condensed mitotic chromosomes (data not
334 shown, see (Hübner, 2020).

335 In a second set of experiments, we studied movements of microinjected 20 nm
336 sized fluorescent nanobeads in nuclei of live C3H 10T1/2 nuclei, where transient
337 transfection of C3H 10T1/2 cells with a construct for the expression of histone H2B
338 tagged with mRFP (Wolff et al., 2006) allowed the visualization of chromatin
339 (Strickfaden et al., 2010). Figure 5f-g shows two nanobeads (green) within such a
340 nucleus at the beginning and the end of a 6h observation period. Figure 5h presents
341 the entire paths travelled by the two nanobeads; Figure 5i indicates that movements
342 occurred most of the time within less dense chromatin (attributed to the ANC), possibly
343 in a random-walk like fashion.

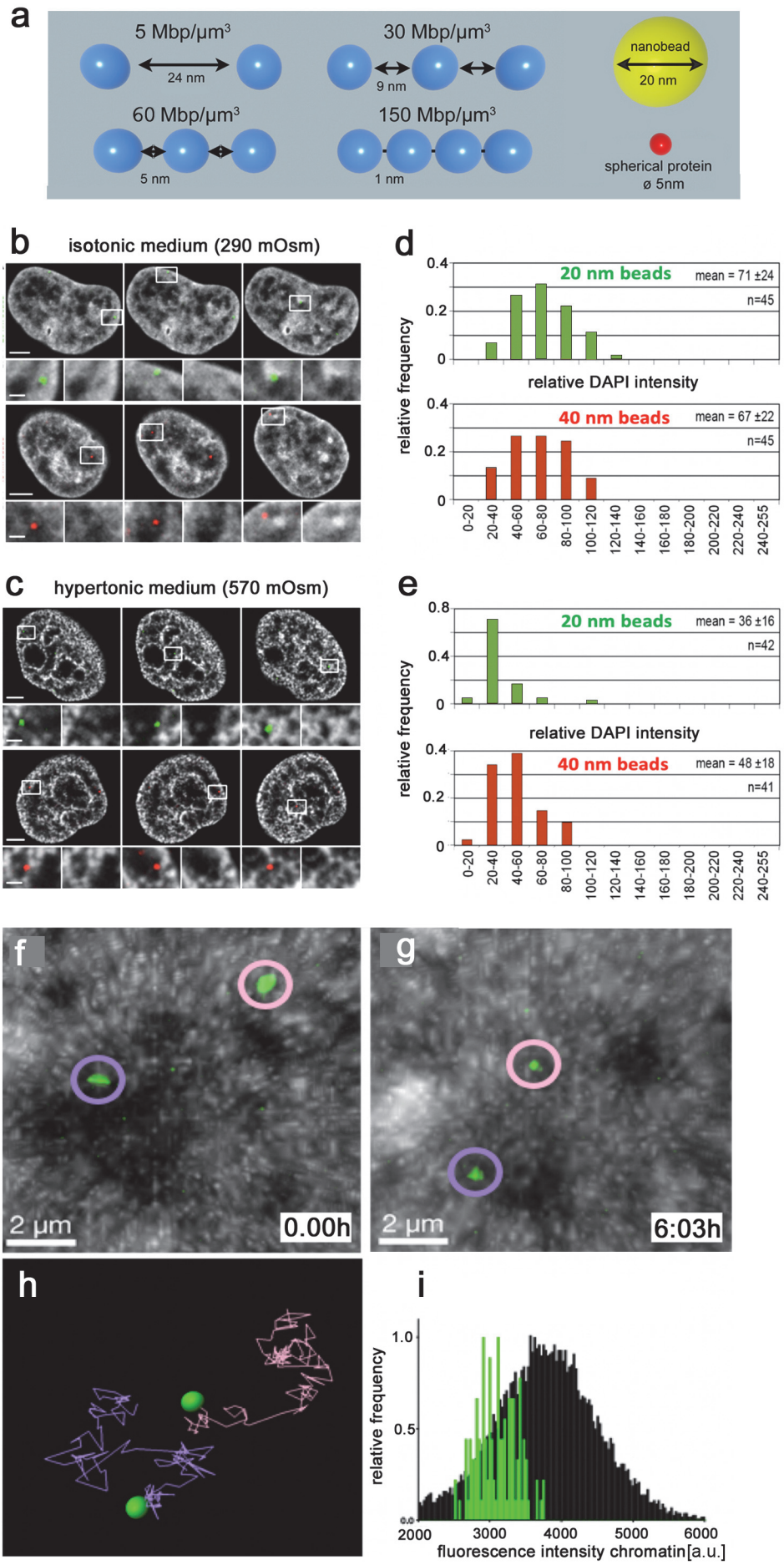
a
5 Mbp/µm³
24 nm
30 Mbp/µm³
9 nm
nanobead
20 nm
60 Mbp/µm³
5 nm
150 Mbp/µm³
1 nm
spherical protein
ø 5nm
b
isotonic medium (290 mOsm)
c
hypertonic medium (570 mOsm)
d
20 nm beads
mean = 71 ±24
n=45
relative DAPI intensity
40 nm beads
mean = 67 ±22
n=45
relative frequency
e
20 nm beads
mean = 36 ±16
n=42
relative DAPI intensity
40 nm beads
mean = 48 ±18
n=41
relative frequency
0-20
20-40
40-60
60-80
80-100
100-120
120-140
140-160
160-180
180-200
200-220
220-240
240-255
f
2 µm
0.00h
g
2 µm
6:03h
h
i
relative frequency
fluorescence intensity chromatin[a.u.]

344

Figure 5: Localization and mobility of microinjected nanobeads within the ANC
a *Distances between surfaces of uniformly arranged nucleosomes (spheres of 10 nm Ø) in 3D space estimated for different DNA densities (5, 30, 60, and 150 Mbp/µm^3), compared to the size of individual macromolecules (Ø 5 nm) and of condensates or macromolecular complexes (Ø 20 nm) (for details see Methods).* ***b-c*** *Live HeLa cells, kept either in isotonic medium (**b**) or hypertonic medium (**c**), were microinjected with 20 nm (green, upper panel) and 40 nm (red, lower panel) fluorescent nanobeads and fixed thereafter with PFA. Nuclear DNA was counterstained with DAPI (gray). 3D confocal serial sections were recorded from microinjected cells, and sections with bright nanobead signals (boxed areas) were selected for further evaluation. Magnifications of the boxed areas (lower rows) show nanobeads located within the IC-lacunae (left) together with the DAPI image alone (right) for comparison. Intensity profiles of line scans through individual nanobeads and across the DAPI stained nuclear landscape were analyzed in 40 nuclei (Supplemental Figures S5 and S6). Scale bars: 4 µm in images of whole nuclei, 1 µm in magnifications.* ***d-e*** *Localization of 20 and 40 nm sized nanobeads as a function of relative DAPI intensities in nuclei of cells kept in isotonic (d) or hypertonic medium (e). In both isotonic and hypertonic nuclei, ≥90% of nanobeads are located in regions with DNA densities ≤100 (gray value range 0-256). Mean values are presented with standard deviation. These data demonstrate the location of nanobeads within less dense DNA attributed to the ANC. For further details see (Hübner, 2020).* ***f-g*** *In vivo labeling of the chromatin of C3H 10T1/2 cells was performed with a fluorescent protein (mRFP) associated with H2B. Dark and light regions show chromatin of low and high densities, attributed to the ANC and INC, respectively. The two green encircled dots indicate the position of two microinjected nanoparticles at the beginning and the end of the observation period.* ***h*** *shows the whole paths travelled by the two nanobeads.* ***i*** *A comparison of relative mRFP intensities (arbitrary units) across the entire nuclear section (black) with intensities at sites of nanobeads (green) supports the hypothesis that nanobeads move within less dense chromatin, attributed to the ANC (compare Supplemental Video S2).*

For a glimpse on dynamic topographical changes between co-aligned ANC and INC ensembles, we conducted DNA pulse labeling experiments during S-phase. These experiments indicate the formation of replication domains within the ANC. Pulse-chase labeling experiments demonstrate replication within wide IC-channels pervading constitutive heterochromatin blocks, followed by the re-location of replicated, inactive chromatin into dense chromatin attributed to the INC (Supplemental Figure S7).

Discussion

In this study, we present examples of nuclear landscapes from a variety of human and mouse cell types imaged with different optical principles (SMLM, SIM and ESI). With

384 SMLM-fBALM, the positions of millions of 'blinking' DNA-bound reporter fluorophore
385 positions (SMPs) in optical nuclear sections were obtained with an average lateral
386 resolution of ~20 nm within the object plane and an axial resolution of ~100 nm.
387 Accordingly, the estimated observation volume (Hell and Stelzer, 1992) was about
388 500x smaller compared to conventional wide-field fluorescence microscopy. High-
389 resolution DNA density maps generated from SMLM-fBALM images revealed absolute
390 DNA compaction differences in nuclei of fixed cell samples from <5 Mbp/μm^3 to >300
391 Mbp/μm^3, a range much higher than previously published (see Introduction).
392 Monte-Carlo simulations (Maeshima et al., 2015) have predicted accessibility
393 constraints for nucleosomal concentrations in the order of 0.3 mM to 0.5 mM, reflecting
394 40 – 60 Mbp/μm^3 in case of DNA fully compacted with nucleosomes. Based on these
395 simulations and our new results, we provisionally attribute chromatin with less dense
396 DNA (<40 Mbp/μm^3) to the active nuclear compartment (ANC), and chromatin with
397 denser DNA (>40 Mbp/μm^3) to the inactive nuclear compartment (INC). Constrained
398 movements of individual macromolecules into the INC may help to increase the
399 concentration of such molecules in the ANC and as a consequence lead to a
400 preferential formation of functionally important macromolecular complexes in the ANC,
401 composed of the interchromatin compartment (IC, and the perichromatin region (PR)
402 (Cremer et al., 2020a). To explore sterical accessibility barriers imposed by densely
403 packaged chromatin attributed to the inactive chromatin compartment (INC), we
404 microinjected fluorescent beads with diameters of 20 nm and 40 nm, reflecting sizes
405 typical for transcription- and replication-complexes, into nuclei of living cells. We
406 observed that movements of these nanobeads were typically restricted to the less
407 dense chromatin of the ANC. These results are consistent with previous live cell
408 fluorescence microscopy of artificial nuclear bodies built up from clustered plasmids
409 with inducible transgenes (Meggendorfer et al., 2010). Artificial bodies were formed

410 within the IC and stayed there during interphase independently of their silent or induced
411 active state, suggesting that their size prevented diffusion into the lining chromatin.
412 Activation of transgene transcription resulted in the recruitment of RNA polymerase II
413 and NFκB and a closer positioning to splicing speckles. Upon entry of cells into mitosis,
414 the bodies were never trapped within, but always separated from mitotic
415 chromosomes.

416 Our new observations together with published results support the hypothesis
417 that functional machineries are size-excluded from the compact interior of chromatin
418 ensembles with DNA densities allocated to the INC (Cremer et al., 2020a; Maeshima
419 et al., 2015). The examples of nuclei shown in this study for a human fibroblast (BJ1),
420 a human cancer cell (HeLa), and a mouse fibroblast (C3H T1/2), support typical
421 architectural features of the ANC-INC model, arguably because these features are
422 indispensable for functional reasons in cell nuclei. Many nucleosome clusters have
423 sizes in the order of ~100 nm or even less and therefore their spatial conformation
424 cannot be further analyzed by microscopy at conventional resolution. In line with our
425 present study, a series of previous microscopic studies with SMLM (Kirmes et al.,
426 2015), and structured illumination microscopy (SIM) (Cremer et al., 2020b; Cremer et
427 al., 2015; Miron et al., 2020) has provided evidence for major functional roles of
428 chromatin ensembles located in the ANC, including transcription and DNA replication
429 (Smeets et al., 2014). In addition to functionally active chromatin ensembles located in
430 the perichromatin region (PR) (Rouquette et al., 2010), chromatin/DNA loops
431 apparently extrude from the PR into the interchromatin compartment (IC). Arguably,
432 large and highly expressed genes in normal cell types (Leidescher et al., 2022), as well
433 as highly expressed amplicons of genes in cancer cells (Solovei et al., 2000), expand
434 along IC-channels through the nuclear space into and even through neighboring CTs.
435 These observations, however, do not contradict the hypothesis that loops formed by

436 most active genes are small-sized. A schematic model of a chromatin domain
437 (Figure 6a adapted from (Miron et al., 2020) argues for small loops with active histone
438 marks (green dots), associated transcription factors and RNA polymerase complexes
439 located at the CD periphery (ANC). In contrast, nucleosomes with repressive histone
440 marks locate within the repressed CD core (INC), where they are inaccessible for the
441 transcriptional machinery. This model implies that transcriptional repression or
442 activation may depend on mechanisms for the 3D re-location and epigenetic
443 remodeling of nucleosomes with important target sequences, such as from the
444 transcriptionally competent CD periphery into the silent interior and vice versa from the
445 interior to the periphery for activation. Notably, such a re-location mechanism allows
446 stochastic heterogeneity of the positions of nucleosomes whose exact positions may
447 be functionally irrelevant, but requires a functionally indispensable preciseness of the
448 space-time organization of CDs only for those nucleosomes which carry important
449 DNA target sequences, such as transcription regulatory elements (Figure 6b) (Cremer
450 and Cremer, 2019). For example, we consider regulatory and coding sequences of
451 active genes located within the ANC in cycling cells. Their relocation into the compact
452 chromatin of the INC in postmitotic, terminally differentiated cells would provide a
453 structural mechanism to safeguard long-term silencing. In case that regulatory
454 sequences of such genes become inaccessible in the interior of highly compact
455 domains, their accessibility would require chromatin decondensation to an extent that
456 allows constrained movements of required transcription factors into the domain
457 interior. Similar structural mechanisms may be envisaged for movements of DNA
458 between neighboring parts of the ANC and INC required for DNA replication.

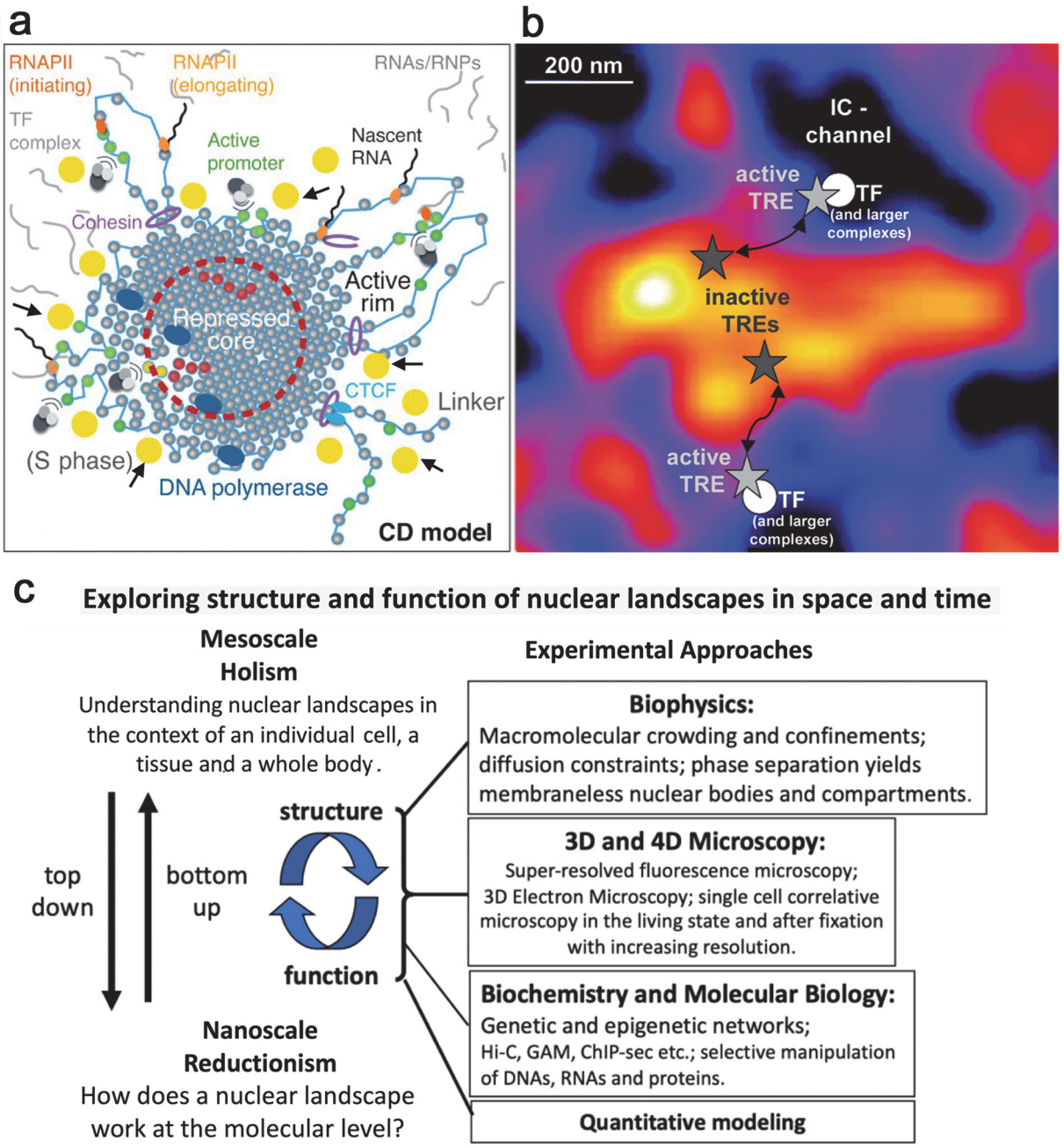

Figure 6: Nanoscale and mesoscale topography of the nuclear landscape

a *Nanoscale model of a chromatin domain adapted from (Miron et al., 2020). It presents a chromatin domain with a repressed core of densely compacted nucleosomes and an active rim with expanding, transcribed chromatin loops. Yellow dots (some of them marked by small arrows) are added to indicate phase-separated, 20-nm sized droplets.* ***b*** *Mesoscale model of functionally interacting active and inactive nuclear compartments (Cremer and Cremer, 2019). The ANC-INC model proposes functional interactions between the ANC and INC based on hypothetical bidirectional chromatin movements, such as genes and corresponding*

468 *transcription regulatory elements (TREs), from the ANC into the INC for long-term silencing,*
469 *and from the INC to the ANC in case of renewed transcriptional activation. In this hypothetical*
470 *nuclear section, the INC is represented by a chromatin domain cluster with several high-*
471 *density peaks (white-yellow) and surrounding slopes (red), embedded within the ANC with its*
472 *much less compacted chromatin. The ANC is composed of transversely cut IC-channels*
473 *(black) and the lining perichromatin region (PR) (blue). Dark stars indicate the location of*
474 *inactive TREs within the INC, light grey stars the position of active TREs in the ANC.* ***c*** *An*
475 *integrative experimental approach to explore the intricate space-time, structure-function-*
476 *conundrums of nuclear landscapes at nanoscale and mesoscale.*
477
478 Still, it is not clear, how chromatin nanostructures form higher levels of chromatin
479 organization (Beagrie et al., 2021; Eltsov et al., 2008; Jerkovic and Cavalli, 2021;
480 Minnoye et al., 2021; Zakirov et al., 2022). For an in-depth understanding of these
481 relationships, it is mandatory to produce fully integrated, high-resolution maps, based
482 on the full range of microscopic/biophysical and biochemical approaches (Figure 6c).
483 Recent evidence has suggested a dual nature of chromatin (Hansen et al., 2021;
484 Strickfaden et al., 2020). The nuclear matrix proteome (Sureka and Mishra, 2021) may
485 form phase-separated droplets within the IC with the help of non-coding RNA
486 sequences (Farabella et al., 2021; Razin and Gavrilov, 2021). Like assembled
487 macromolecular machineries, such condensates are excluded by size from the INC
488 and may serve as storage vesicles for the formation of functional machineries. For
489 example, scaffold attachment factor A (SAF-A), was observed in the ANC (Smeets et
490 al., 2014). Transitions between liquid and solid states of chromatin ensembles are still
491 not well understood (Hansen et al., 2021). Whereas constrained local motions of
492 nucleosomes occur on the seconds timescale, solid chromatin at mesoscale does not
493 mix with its environment on the minutes to hours timescale. Phase-separation has

494 been implicated in euchromatin and heterochromatin formation in a complex interplay
495 with epigenetic mechanisms (Rowley and Corces, 2018). Chromosome territories
496 apparently form a polymer network with material properties of an elastic hydrogel
497 (Hansen et al., 2021). While a liquid state of 200 nm sized chromatin domains would
498 enable the efficient activation of genes through diffusion-mediated, long-range
499 regulatory contacts, the possibility that 200 nm domains exist as a solid gel state and
500 exert gel-like sieving effects may also be considered. Evidence for a gel-like chromatin
501 organization at mesoscale suggests a porous structure of the chromatin landscape
502 with sieving effects affected by global or linear shapes of diffusing macromolecules
503 (Cai et al., 2015; Pluen et al., 1999; Seelbinder et al., 2021). Phase-separated droplets,
504 carrying an assembly of macromolecules (proteins, non-coding RNAs) required for
505 specific nuclear functions, may interact with chromatin domains with gel-like properties.
506 Such complex interactions are not explained by models of an exclusively size-
507 dependent accessibility. For example, the penetration of small macromolecules
508 assembled within such droplets into the interior of dense chromatin may be prevented,
509 whereas percolation of individual, larger macromolecules is still possible.

510 A recent polymeric model of higher order chromatin arrangements at mesoscale
511 was based on phase separation of chromatin, considering two key features, namely
512 chromatin self-attraction and its binding to the peripheral lamina (Amiad-Pavlov et al.,
513 2021; Bajpai et al., 2021). It offers a biophysical mechanism for the overall
514 determination of nuclear chromatin density and hence accessibility by the regulation
515 of lamina-chromatin interaction strength. Such a quantitative numerical model may
516 help in part to explain physical properties of the ANC-INC model (Cremer et al., 2020b;
517 Cremer et al., 2020a; Schmid et al., 2017). Other polymeric models provide similar
518 interaction principles to control the density and hence accessibility of individual gene
519 domains (Chiariello et al., 2016). Computer models of chromatin nanostructures

520 performed under various biochemical assumptions, such as histone linker length, Mg^{2+}
521 concentration, acetylation, histone interactions, or epigenetic marks argue for highly
522 complex nanostructures containing relatively open parts as well as small regions with
523 an apparent chromatin density sufficiently high to constrain the access of individual
524 macromolecules, likely preventing the penetration of larger aggregates (Bascom et al.,
525 2016; Odenheimer et al., 2009; Paulsen et al., 2018; Rosa and Zimmer, 2014). Schlick
526 and colleagues (Bascom et al., 2019) performed numerical simulations based on Hi-C
527 and epigenetic data of the 55 kbp-sized HOXC gene for a series of 3D configurations
528 representing inactive and active chromatin states, compare Figure S3 in (Bascom et
529 al., 2019). Extended model configurations show highly condensed clusters of densely
530 packed nucleosomes connected by stretches of nucleosome-free DNA, i.e., highly
531 accessible sites. From the volumes within the enveloping surfaces of these ensembles,
532 one can estimate average densities ranging from ~7 Mbp/μm^3 to ~20 Mbp/μm^3. These
533 average estimates, however, do not allow conclusions about the actual densities of
534 structures below the resolution limit. Direct imaging of such structures remains an
535 unsolved challenge and would likely require an intranuclear 3D structural resolution of
536 a few nm.

537 Constrained spatial accessibility due to dense chromatin compaction of the INC
538 is not the only barrier preventing/attenuating the diffusion of proteins and RNAs from
539 the nucleosome free space of the ANC into the INC (Imai et al., 2017). Other features,
540 such as electric charge (Cremer et al., 2000) and the enrichment of macromolecules
541 within phase-separated droplets, may also affect the accessibility of chromatin
542 ensembles. In addition, for more sophisticated models of chromatin accessibility, it
543 would be important to achieve more information about the space-time distribution of
544 nucleosomes (Baldi et al., 2020; Kharerin et al., 2020). To which extent dense
545 convolutes of naked DNA may exist in the ANC has remained elusive.

546 True-to-scale DNA density maps should be complemented by similar density
547 maps based on nucleosome positions as an essential basis for modeling of chromatin
548 accessibility. Ideally, one would like to follow the dynamics of any target sequence of
549 interest within a given chromatin ensemble and explore in living cells the dynamic
550 compaction of individual loops or nanodomains comprising a few kb and the potential
551 opening and closing of IC-channels. The generation of such space-time nuclear maps
552 requires the development of time-resolved super-resolution microscopy approaches of
553 live cells (Chu et al., 2021; Ricci et al., 2015; Shechtman et al., 2017; Wombacher et
554 al., 2010; Xiang et al., 2018). The space-time visualization of chromatin ensembles is
555 essential for studies to solve the question of intermingling loops between neighboring
556 CTs (Branco and Pombo, 2006; Rouquette et al., 2010). Furthermore, an appropriate
557 toolset should allow the integration of epigenetic marks, RNAs and non-histone
558 proteins into individual chromatin ensembles across the entire nuclear landscape
559 (Barth et al., 2020; Ma et al., 2016). Steadily improved, color-coded, high-resolution
560 maps of nuclear landscapes are ideally suited to incorporate huge datasets of
561 additional genetic and epigenetic information in an intelligible manner, providing direct
562 insight into the interdependence of structural and functional changes (Gorkin et al.,
563 2020; Lohoff et al., 2022; Yang et al., 2021). This is a long way to go not only with
564 regard to the challenges of developing high resolution 4D live cell microscopy but also
565 in view of the requirements of comprehensive, high-throughput 4D image analyses of
566 large cell numbers. Changes of nuclear landscapes during differentiation and
567 development of numerous cell types provide an important enrichment to the Human
568 Biomolecular Atlas Program (Snyder et al., 2019). Evolutionary comparisons will shed
569 new light on the origin of cell nuclei (Cremer et al., 2018) and the evolution of metazoan
570 chromosomes (Simakov et al., 2022). Based on the emerging evidence that physical
571 compaction and decompaction of chromatin nanodomains play a major role in gene

572 regulation not only in eukaryotes but also in prokaryotes (Swygert et al., 2021), it is
573 interesting to explore to which extent differences between high-resolution DNA density
574 maps of different cell types (Yang et al., 2021) correlate with and may predict global
575 transcriptional differences. Arguably, 3D nuclear arrangements of active and silent
576 genes and their regulatory sequences within active and inactive nuclear compartments
577 may be closely related with a cell's transcriptome and protein interactome at a given
578 time (Nussinov et al., 2021). If so, high resolution DNA-density maps of nuclei in a
579 tissue may serve as structural markers reflecting different functional states (Lang et
580 al., 2021).
581
582 **Limitations of the study**
583 We currently lack equipment for an automated fBALM recording of large numbers of
584 nuclei and algorithms for rapid image analyses. These prerequisites must be met for
585 broad applications of our approach in research and diagnostic settings. The current
586 structural resolution of SMLM (~20 nm lateral, ~100 nm axial) still prevents imaging of
587 chromatin loops at the level of individual nucleosomes. Although our fixation protocols
588 maintain 3D structures of chromatin ensembles to a remarkable extent down to the
589 resolution limit of 3D-SIM (~100 nm lateral, ~250nm axial) (Markaki et al., 2013), we
590 cannot rule out fixation artifacts at higher resolution. Live cell studies of nuclear
591 landscapes with SMLM are currently impractical because the sequential recording of
592 large numbers of frames for high resolution image reconstruction implies motion blur,
593 while fewer frames imply sparse sampling and hence strongly reduced temporal and
594 spatial resolution (Lelek et al., 2021; Schermelleh et al., 2019).
595

596 **Acknowledgments**

597 Márton Gelléri, Shih-Ya Chen, Aleksander Szczurek, Jan Neumann, and Christoph
598 Cremer were supported by the Boehringer Ingelheim Foundation and the Max Planck
599 Institute for Chemistry, Mainz (Germany). Hilmar Strickfaden and Michael J. Hendzel
600 were supported by grants from the Canadian Cancer Research Society (grant number
601 CRISDI 2018 OG 23446) and the Canadian Institutes of Health Research (grant
602 number PJT-148753). The Spinning Disk Confocal System (VisiScope, 5-Elements,
603 IMB Microscopy Core Facility) and the High-Content Screening System (Opera Phenix,
604 Perkin Elmer, IMB Microscopy Core Facility) were supported by the Deutsche
605 Forschungsgemeinschaft (INST 247/912-1FUGG and INST 247/845-1 FUGG). We
606 gratefully acknowledge the support of the Center of Advanced Light Microcopy (CALM)
607 of the LMU Biocenter (headed by Heinrich Leonhardt and Hartmann Harz), for
608 recording SIM images. We are obliged to many colleagues for helpful suggestions. In
609 particular, we thank in alphabetical order Udo Birk, Giacomo Cavalli, Jonas Cremer,
610 Mario Nicodemi, Thoru Pederson, Katharina Ribbeck, Karsten Rippe, Vassilis Roukos,
611 Samuel Safran, and Nadine Vastenhouw for critical reading and discussion. We thank
612 Sandra Ritz and all the members of the IMB Microscopy Core Facility for technical
613 support.

614

615 **Author contributions**

616 CC, HS, MG, MC and TC planned this study and wrote the manuscript. All authors
617 contributed to the final text. S-Y C and CC developed the SMLM instrumentation; AS
618 developed the fBALM approach and contributed experimental SMLM results. SMLM-
619 images of nuclear landscapes were recorded by S-Y C, MG, HS, and AS, electron
620 spectroscopic images by HS. Quantitative Voronoi-analyses of SMLM sections were
621 carried out by MG, analysis of ESI images by HS and MH. Evaluation algorithms were

622 provided by MG, JN, OK, FS, HS and JI. These authors also contributed to the various
623 approaches of SMLM image displays and analyses. Microinjection experiments with
624 fluorescent nanobeads and quantitative analyses were conducted by BH and HS. EdU-
625 replication-labeling experiments with SMLM were performed by AS. MS carried out 3D
626 SIM studies of EdU-pulse-chase experiments with guidance from YM.

627
628
629 ## Material & Methods

630 **Cell cultures, fixation, and staining protocols**

631 h-TERT BJ1 cells, an immortalized diploid human cell line from human foreskin
632 fibroblasts (ATCC #CRL-2522); HeLa cells, a human cervix carcinoma derived cell line
633 with a near-triploid karyotype (Landry et al., 2013), and C3H 10T1/2 cells, derived from
634 a murine embryo fibroblast cell line (ATCC #CCL-226) (Bairstow and Heidelberger,
635 1975) were cultured in DMEM with 5% CO_2 at 37 °C. Undifferentiated female mouse
636 embryonic stem cells (ESC line 16.7, 42,XX; +6;+8, kindly provided by J. Lee, Harvard
637 Medical School) were cultivated under feeder-free conditions on gelatinized cover slips
638 in KO-DMEM (Invitrogen) as described in details in (Smeets et al., 2014). After fixation
639 with formaldehyde (4%) for 15-30 min, cells were kept in Dulbecco's Phosphate
640 Buffered Saline (DPBS, Sigma Aldrich) and incubated with 0.5 U/ml RNase A and 20
641 U/ml RNase T1 (Ambion, USA) for 1 h at 37 °C. It is essential to keep living cells in
642 their normal osmotic environment (Albiez et al., 2006) and avoid drying out of
643 preparations during fixation and all subsequent steps until embedding for microscopic
644 examination in order to maintain the shape, volume and internal structure of cells as
645 best as possible. We employed protocols that maintain 3D nuclear shape and
646 topography of CTs, nuclear speckles, replication domains and 3D positions of genes
647 to a remarkable extent down to the lateral and axial resolution limit of 3D-SIM (x,y ~

648 100 nm and z ~ 250nm) (Markaki et al., 2013). A recent study performed with live and
649 fixed Drosophila larva muscle nuclei found that the live nucleus preserved its volume
650 and ellipsoidal shape, whereas the fixed nucleus exhibited substantial flattening,
651 forming a disk-like shape (Amiad-Pavlov et al., 2021). This flattening effect, however
652 was not observed in our present study (Supplemental Figure S8). In 3D-SIM studies
653 live and fixed cells showed a high degree of similarity with regard to chromatin clusters,
654 sites of decondensed chromatin, IC lacunae and IC channels leading to nuclear pores.
655 A significant impact of fixation artifacts on large-scale chromatin organization was
656 excluded in 3D-SIM live-cell experiments with HeLa cells stably expressing histone
657 H2B-GFP (see additional file 8 in (Smeets et al., 2014). Still, we cannot exclude the
658 possibility of fixation artifacts of active and inactive chromatin ensembles at nanoscale
659 below the resolution limit of 3D SIM.

660 For DNA staining the following dyes were used: Sytox Orange or Vybrant Violet
661 for SMLM-fBALM (fluctuation assisted Binding Associated Localization Microscopy
662 Mode (Chen et al., 2018; Szczurek et al., 2018; Szczurek et al., 2017; Zurek-Biesiada
663 et al., 2016), see below. These dyes were present at a concentration of 0,5 µM
664 throughout the whole imaging procedure. For other microscopic approaches (wide-
665 field, confocal and structure illumination), nuclei were pre-stained with DAPI (5 µg/ml
666 for at least 5 min) and Hoechst (10µg/ml; for at least 5 min) and washed in PBS before
667 use. With a size in the 1 nm range, the accessibility of all dyes should not be
668 substantially impaired by chromatin compaction per se.

669

670 **Determination of cell cycle & nuclear morphology**

671 Determination of cell cycle stage and nuclear morphology of BJ1 and HeLa cells was
672 performed using a spinning disk Opera Phenix Plus High-Content Screening System
673 (PerkinElmer), according to (Roukos et al., 2015), with Sytox Orange as a DNA stain.

674 If not stated otherwise, nuclei corresponding to G1 were used for SMLM-fBALM
675 imaging (Supplemental Figure S2). Imaging was performed in wide field mode with a
676 20x, 0.4 NA objective to capture fluorescence from interphase cells and mitotic cells
677 without the need of recording a z-stack. In each well, multiple images were acquired,
678 covering approximately 80 percent of a single well resulting in 20,000 to 80,000 imaged
679 cells per well. Nuclear area and fluorescence intensity of Sytox Orange was analyzed
680 by segmentation with Harmony software (PerkinElmer). Nuclei that were touching the
681 image border were excluded from further analysis. The frequency distribution of Sytox
682 Orange intensities showed discrete G1 and G2 cell cycle populations that allowed the
683 classification of each cell nucleus into these classes.
684

685 **Microinjection of fluorescent nanobeads (FluoSpheres)**

686 Microinjection of carboxylate-modified FluoSpheres (ThermoFisher Scientific) with a
687 diameter of 20 nm and 40 nm into nuclei was performed on an Axiovert 200 M widefield
688 microscope (Zeiss) with an injection system from Eppendorf. Needles were pulled from
689 borosilicate glass capillaries with an outer diameter of 1.0 mm and an inner diameter
690 of 0.5 mm using a micropipette puller (Sutter Instrument P-97; for details see (Hübner,
691 2020).
692
693 **Pulse-labeling of replication domains (RDs) with EdU**
694
695 For SMLM experiments, RDs were identified following pulse-labeling of HeLa cells for
696 15 min with 5-Ethynyl-dU (EdU) at a final concentration of 10 µM as described (Cremer
697 et al., 2020b; Kirmes et al., 2015). After fixation of cells with 4% formaldehyde/PBS for
698 ~20 min and permeabilization with 0.5% Triton X-100/PBS/0.02% Tween for 10 min,
699 EdU was conjugated to azid modified AlexaFluor 555 and detected by click-chemistry
700 according to manufactures instructions (https://www.thermofisher.com/). DNA was

701 stained with Vybrant Violet (0.5 μM). For 3D-SIM experiments, RDs in mouse
702 embryonic stem cells were identified by an EdU pulse of 10 min. Cells were fixed
703 immediately thereafter with 2% formaldehyde, or after a chase of 20 - 80 minutes and
704 permeabilized with 0.5% Triton X-100/PBS/0.02% Tween for 10 min. EdU was
705 conjugated to azid modified AlexaFluor 488 and detected by click-chemistry according
706 to manufactures instructions (https://www.thermofisher.com/). After post-fixation in 4%
707 formaldehyde for 10 min DNA was counterstained with DAPI (5 µg/ml).
708

709 **Distances between surfaces of uniformly arranged nucleosomes in 3D space**
710 **estimated for different DNA densities**

711 We assumed that the entire genome was fully packaged with nucleosomes, i.e. that
712 each consecutive 200 bp DNA segment carried a nucleosome with ~150 bp of DNA,
713 wrapped around the core histone complex, and a linker length of ~50 bp between any
714 two linearly adjacent nucleosomes located on the same ~10 nm nucleosomal chain. In
715 case of fully extended linker DNA, this means a maximum surface-to-surface distance
716 of ~15 nm. Next, we determined the maximum number and spatial distribution of
717 nucleosomes that can be placed at a given DNA density into a 1 μm^3 cube under the
718 highly simplified assumption of homogenously distributed, equidistant nucleosomes.
719 Placing each nucleosome (represented by spheres with 10 nm diameter) with its center
720 into a sub-cube, we calculated the center-to-center 3D distances between adjacent
721 nucleosomes placed in the midst of these sub-cubes; from this, the minimum average
722 3D distances between the surfaces of spatially adjacent spherical nucleosomes were
723 determined for average DNA densities of 5, 30, 60 and 150 Mbp/μm^3. For example, a
724 cube of 1 μm^3 with an average DNA density of 150 Mbp/μm^3 contains ~750,000
725 nucleosomes placed at a mean 3D distance of ~1 nm between the surfaces of any two
726 nucleosome neighbors adjacent in 3D space. In contrast, a 1 μm^3 cube with an average

727 DNA density of 5 Mbp/μm^3 contains only ~25,000 nucleosomes with a minimum 3D
728 distance of ~24 nm. Note that many next nucleosome neighbors in 3D space may be
729 located at different DNA sites of the same nucleosomal chain or on different spatially
730 adjacent loops. This explains why the minimum average distance calculated for 5
731 Mbp/μm^3 exceeds the maximum length of ~15 nm for a fully stretched 50 bp DNA
732 linker.

733 These estimates cannot replace sophisticated modeling, taking into
734 consideration the constraints of polymer chain folding of 10 nm thick nucleosomal
735 chains (Amitai and Holcman, 2017). Notably, highly compacted chromatin does not
736 provide much freedom for local changes of accessibility resulting from a dynamic, non-
737 uniform distribution of nucleosomes. Whereas the accessibility of the interior of a loop
738 forming a dense nucleosome cluster is highly constrained (Maeshima et al., 2015),
739 such constraints may barely matter in case of an open loop configuration (compare
740 Figure 1c).

741

742 **Single Molecule Localization Microscopy (SMLM)**

743 For studies of high-resolution DNA density maps with SMLM-fBALM (fluctuation-
744 assisted Binding Activated localization microscopy) mode (Szczurek et al., 2018;
745 Szczurek et al., 2017) an inverse custom-made localization microscope was equipped
746 with three lasers emitting at 488 nm, 561 nm and 647 nm. The three lasers were
747 combined with dichromatic reflectors. The laser beams were expanded by a pair of
748 lenses and focused to the back focal plane of the objective lens (HCX PL APO 100x/NA
749 1.47 oil, Leica, Germany) by a tube lens. A quadband dichroic mirror was used to
750 reflect the laser and to transmit emitted fluorescence light from the sample. In this
751 setup, a Gaussian intensity distribution with a full width at half maximum (FWHM) of
752 50 μm was created in the focal plane of the objective lens.

753 fBALM relies on the spatial switching of fluorescent on/off states by adjusting
754 the local environment of the DNA and DNA-binding sites. The chemical environment,
755 in particular the pH value, allows control over the local, reversible DNA melting of
756 double stranded into single stranded DNA. Sytox Orange binds to dsDNA, falls off after
757 local melting from ssDNA, and rebinds to dsDNA, usually at another site. Unbound
758 Sytox Orange molecules have a fluorescence up to several orders of magnitude lower
759 than the emission of blinking DNA-bound molecules. Furthermore, unbound Sytox
760 Orange molecules have a much larger mobility. Hence their weak fluorescence
761 emission forms a rather homogeneous background which can be removed by
762 appropriate image analysis tools (Kaufmann et al., 2009). In summary, fBALM provides
763 both a substantial reduction of background combined with a very high number of
764 blinking events of dsDNA bound fluorophores, which is only limited as a consequence
765 of either complete bleaching of the entire pool of Sytox Orange molecules, a change
766 of the chemical environment, or of an optical instability of the SMLM setup.

767 SMLM-fBALM allowed the determination of single-molecule positions (SMPs) of
768 Sytox Orange molecules in nuclei with a typical average precision of σ_{xy} ~8 - 15 nm
769 (object plane; best values around 2 nm in heterochromatic regions), and an axial
770 precision σ_z down to about 50 nm. From these figures, an average lateral optical
771 resolution OR_{xy} (smallest lateral distance detectable between two molecule positions)
772 of 20 nm was obtained for σ_{xy} = 8.5 nm, and around 100 nm for OR_z along the optical
773 axis. For molecule positions with a localization precision (object plane, xy) of 2 nm, the
774 best OR_{xy} value estimated was around 5 nm. Experimentally, in nuclear sections of
775 HeLa nuclei, selected single molecule positions with σ_{xy} ≤5 nm and mutual xy-
776 distances of 11 nm and of 14 nm, respectively, were clearly distinguished. For the
777 object plane coordinates with σ_{xy} = 8.5 nm and d (SMPs/nuclear area = 10^7/100 μm^2 =
778 0.1/nm^2), the average structural resolution R (as a measure for the smallest observable

779 structure) was estimated according to $R = [(2.35\ \sigma_{xy})^2 + (4/d)]^{0.5}$ (Cremer et al., 2017).
780 From this, R = 21 nm was obtained if all 10 million molecule positions localized are
781 included in a 600 nm optical section. For a thinner optical section of about 100 nm with
782 1.5×10^6 molecule positions, R = 26 nm was estimated. If in addition the average drift
783 (after correction) is included (Zurek-Biesiada et al., 2016), then the average R
784 increases from 21 nm to 23 nm, and from 26 nm to 28 nm, respectively.

785 Selected HeLa and BJ1 cells were placed in the center of the field of view of the
786 inverted SMLM-microscope. Nuclei were exposed to the 561 nm laser at an estimated
787 illumination intensity of about 1 kW/cm^2. Fluorescence was collected by the objective
788 lens and was separated from the excitation laser by a dichromatic beam splitter and
789 appropriate emission filters. The emission light was focused by a second tube lens and
790 imaged on an sCMOS camera (PCO edge 4.2) with a pixel size corresponding to
791 65 nm in the object plane, setting the exposure time to 50 ms/frame. Up to 50,000
792 frames with a total of ~10 million blinking events were recorded in a single ~600 nm
793 thick light optical section and localized with appropriate localization algorithms (Cremer
794 et al., 2017; Kaufmann et al., 2009). The possibility that the same fluorophore was
795 recorded twice (double blinking event) was considered in cases where two signals
796 recorded in subsequent image frames had a distance smaller than 20 nm. These rare
797 events were excluded from further image analysis as described below. To localize
798 SMPs from a thinner section than 600 nm, achieved with conventional wide-field
799 resolution, a cylindrical lens was placed in front of the sCMOS camera (Chen et al.,
800 2018) to induce an astigmatism (Huang et al., 2008). In this way it was possible to
801 assign SMPs to positions ± 50 nm above or below the focal plane and thus filter out
802 the SMPs in a ca. 100 nm thick optical section (assumed to be ca. 1/6th of the total
803 number of SMPs in the 600 nm optical section).

804 For recording of DNA densities and replication domains (RDs) with dual-color
805 SMLM, a custom-built, upright-setup (Reymann et al., 2008) was used, equipped with
806 lasers for excitation wavelengths 405 nm and 491 nm, respectively (Zurek-Biesiada et
807 al., 2016). EdU-labeled RDs were conjugated to AlexaFluor 555 and recorded first
808 (5,000 SMLM frames). Vybrants DyeCycle™ Violet (VdcV) was used to label the non-
809 replicated DNA (Zurek-Biesiada et al., 2016). After photoconversion with 405 nm,
810 Vybrant Violet was excited to 'blink' by intense 491 nm illumination, and the emitted
811 green fluorescence was registered (30,000 frames).
812
813 **Estimation of true-to-scale DNA density values**
814 The procedure we have used to achieve true-to-scale DNA density values is illustrated
815 in Supplemental Figure S3 using the BJ1 light optical section presented in Figure 2.
816 The reliability of 3D DNA density values for a given chromatin ensemble critically
817 depends on the determination of both its absolute DNA content and its volume. Several
818 essential requirements for precise measurements of these values need to be
819 considered.
820 First, our concept assumes that Sytox Orange (Szczurek et al., 2018) binds
821 randomly, i.e. without base-pair preference, to the nuclear dsDNA, and can be
822 localized with high precision by SMLM. The lateral nuclear positions of SMPs (within
823 the object plane) were determined with an average precision of 8 - 15 nm. This requires
824 extreme mechanical stability of the microscopic setup (Chen, 2020; Chen et al., 2019).
825 The determination of the axial positions of SMPs (Chen et al., 2018) was not further
826 defined, but assumed to reflect the thickness of the light optical section, which was
827 about 600 nm in the example HeLa cell nucleus (Figure 3). In the case of the BJ1
828 nucleus (Figure 2) and HeLa nucleus (Figure 3), the use of an astigmatic lens (Huang
829 et al., 2008) resulted in an improved axial localization precision of SMPs down to about

830 50 nm in a 100 nm thick optical section. Under optimal conditions, lateral nuclear SMP
831 distance differences <5 nm were detected. The pixel size for the density determination
832 was adapted to reflect the mean localization precision of the SMLM measurements.
833 For volume estimates of light optical sections, we assumed a thickness of 100 nm in
834 SMLM setups with an achromatic lens and of 600 nm without such a lens.

835 Second, for estimates of the total DNA content of an entire nucleus or a given
836 light optical section, it is necessary to determine the interphase stage of the studied
837 cell. Cell cycle measurements (see above) indicated that the cells subjected to fBALM
838 were in G1. In the case of cells with an abnormal chromosome content, such as HeLa
839 cancer cells, it is preferable to measure the DNA content of a single, studied cell
840 nucleus (not performed here) or to provide an estimate based on knowledge of the
841 karyotype, though this karyotype may differ from cell to cell. For BJ1 cells we assumed
842 a diploid karyotype (2n), and for HeLa cells a near triploid karyotype (3n).

843 Third, the calibration of absolute DNA density values should ideally be based
844 on the total number of SMPs mapped within an entire cell nucleus. This total number
845 then reflects the total DNA content. Accordingly, the fraction of genomic DNA
846 represented by a single SMP can be calculated. Ideally, this approach would require
847 high resolution, optical serial sectioning of a given nucleus with SMLM-fBALM in order
848 to sum up the total number of blinking events and determine its shape and volume
849 together with its total DNA content. In practice, the decrease of blinking efficiency due
850 to a deterioration of the chemical switching conditions (Szczurek et al., 2017) during
851 the long registration times prevented serial SMLM sections of entire nuclei with high
852 structural resolution. For this reason, we typically determined the height of the nucleus
853 given by the distance between the top and bottom section and performed a single
854 SMLM midsection from nuclei with a high average SMP density. For simplicity, we
855 assumed a homogeneous DNA distribution, yielding a linear relationship between

856 volume and DNA content. Furthermore, we assumed that the shape of a nucleus
857 conforms to a cylinder with a circular or elliptical base and the specified height.
858 Fourth, calibration of the amount of DNA represented by each SMP in a given
859 section allows estimates of the absolute DNA density of a given chromatin ensemble,
860 recorded in this section. For this purpose, it is necessary to count the number of SMPs
861 attributed to such an ensemble. This is easy in cases, where the outline of an ensemble
862 can be precisely determined, for example after FISH of DNA targets with specific
863 probes (Bintu et al., 2018; Weiland et al., 2011). In the absence of further information,
864 however, demarcation of individual ensembles, say a chromatin loop, a chromatin
865 domain, or a chromosome territory, from neighboring structures, is difficult and often
866 impossible. Using a customized version of a published Voronoi algorithm (Andronov et
867 al., 2016), we dissected the cloud of SMPs into Voronoi areas limited by lines with
868 equal distances to neighboring SMPs. The smaller the distances between neighboring
869 SMPs, the smaller were the defined Voronoi areas, and the higher was the estimated
870 density of SMPs. This approach was performed without any density thresholding based
871 on biological assumptions about chromatin ensembles with specific structural or
872 functional properties. Based on Voronoi area frequencies we generated a histogram
873 of the DNA density distribution across a given optical section. Based on the calibration
874 between the number of SMPs and the corresponding DNA content, histograms of
875 Voronoi area frequencies were converted into a color-coded map of absolute DNA
876 densities (Mbp/μm^3). However, this advantage was achieved at a cost: Voronoi
877 tessellation is particularly useful to detect local DNA densities, likely corresponding to
878 small nucleosome clusters, but fails to detect chromatin loops formed by extended ~10
879 nm thick nucleosomal chains or naked DNA.
880
881 **3D-Structured Illumination Microscopy (SIM)**

882 Super-resolution imaging of fixed cell samples with 3D-SIM was performed on a
883 DeltaVision OMX V3 system (Applied Precision Imaging/GE Healthcare) equipped with
884 a 100x/1.40 NA PlanApo oil immersion objective (Olympus), Cascade II:512 EMCCD
885 cameras (Photometrics) with 405 and 488 nm diode lasers. 3D-SIM image stacks were
886 acquired with a z-distance of 125 nm and with 15 raw images per plane (5 phases, 3
887 angles). The raw data was then computationally reconstructed using Wiener filter
888 settings 0.002 and channel-specifically measured optical transfer functions (OTFs)
889 using the softWoRX 6.0 software package (Applied Precision) to obtain a super-
890 resolution 3D image stack with a lateral (xy) resolution of ~120 nm and an axial (z)
891 resolution of ~300 nm. The level of spherical aberration was minimized and matched
892 to the respective OTFs using immersion oil with different refractive indices (RI)(Smeets
893 et al., 2014). Images from the different color channels were registered with alignment
894 parameters obtained from calibration measurements with 0.2 µm diameter TetraSpeck
895 beads (Invitrogen). The reconstruction process generates 32-bit data sets with the
896 pixel number doubled in the lateral axes, and the lateral pixel size halved from 80 nm
897 to 40 nm in order to meet the Nyquist sampling criterion. To normalize all image stacks
898 for subsequent image processing and data analysis, the stack-specific mode gray
899 value (representing the peak of the background noise) was subtracted, negative values
900 discarded and finally the format converted to 16-bit composite tiff-stacks using a
901 custom-made script based on ImageJ (http://rsbweb.nih.gov/ij).
902

903 **Confocal microscopy of microinjected nanobeads**

904 For confocal microscopy of microinjected nanobeads, a laser scanning and a spinning
905 disk confocal microscope were used. The TCS SP5 DMI 6000 CS CLSM microscope
906 (Leica Microsystems, Mannheim/Germany) was equipped with a HCX Plan
907 Apochromat Lambda Blue 63x/1.4 oil objective lens and various laser sources, the

908 excitation wavelengths ranging from 405 nm to 633 nm. Spinning disk confocal
909 microscopy was performed on an Ultraview system (PerkinElmer) equipped with
910 405 nm, 488 nm, and 561 nm diode lasers using a 100x/1.4 oil Apochromat (Zeiss)
911 objective lens.
912
913 **Electron Spectroscopic Imaging (ESI)**
914 C3H 10T1/2 growing in 35mm MatTek glass bottom dishes cells were fixed in 0.1 M
915 Phosphate Buffer containing 4% paraformaldehyde and 2% glutaraldehyde for 30 min.
916 Then the cells were permeabilized with 0.1% Triton X-100 for 15 min. After washing
917 with 1xPBS the cells were treated with RNAse as described above. After a dehydration
918 series (50%, 70%, 90%,100%) each 30 min, the cells were infiltrated with acrylic resin
919 (LR White) (1:1 mixture with 100% ethanol for 4h and in pure LR White overnight).
920 Placing an LR White filled 2 ml Eppendorf tube on top of the cells and polymerizing the
921 acrylic resin for 48h at 65°C in the oven, blocks were created that could after detaching
922 from the glass be trimmed and cut with a Diatome diamond knife on a Leica Ultracut
923 UC6 microtome (Strickfaden et al., 2015). 100 nm ultrathin sections were picked up on
924 300 Mesh copper grids and carbon coated. Cells were located in a JEOL F2100
925 transmission electron microscope. Phosphorous and nitrogen elemental maps were
926 recorded using a GATAN Quantum post column electron energy loss spectrometer
927 equipped with a GATAN UltraSCAN 1000 CCD camera. For phosphorous elemental
928 maps, post-edge pictures were recorded at 162.5 eV (slit width 20 eV) and pre-edge
929 images at 119.5 eV and 99.5 eV (slit width 20 eV each) (3-window method). For
930 nitrogen elemental maps, post-edge pictures were recorded at 416 eV (slit width) and
931 pre-edge pictures were recorded at 416 eV and 383 eV (slit width 30 eV each).
932 Phosphorous and nitrogen elemental maps were computed in Digital Micrograph by
933 GATAN.

934 **Supplementary Information**

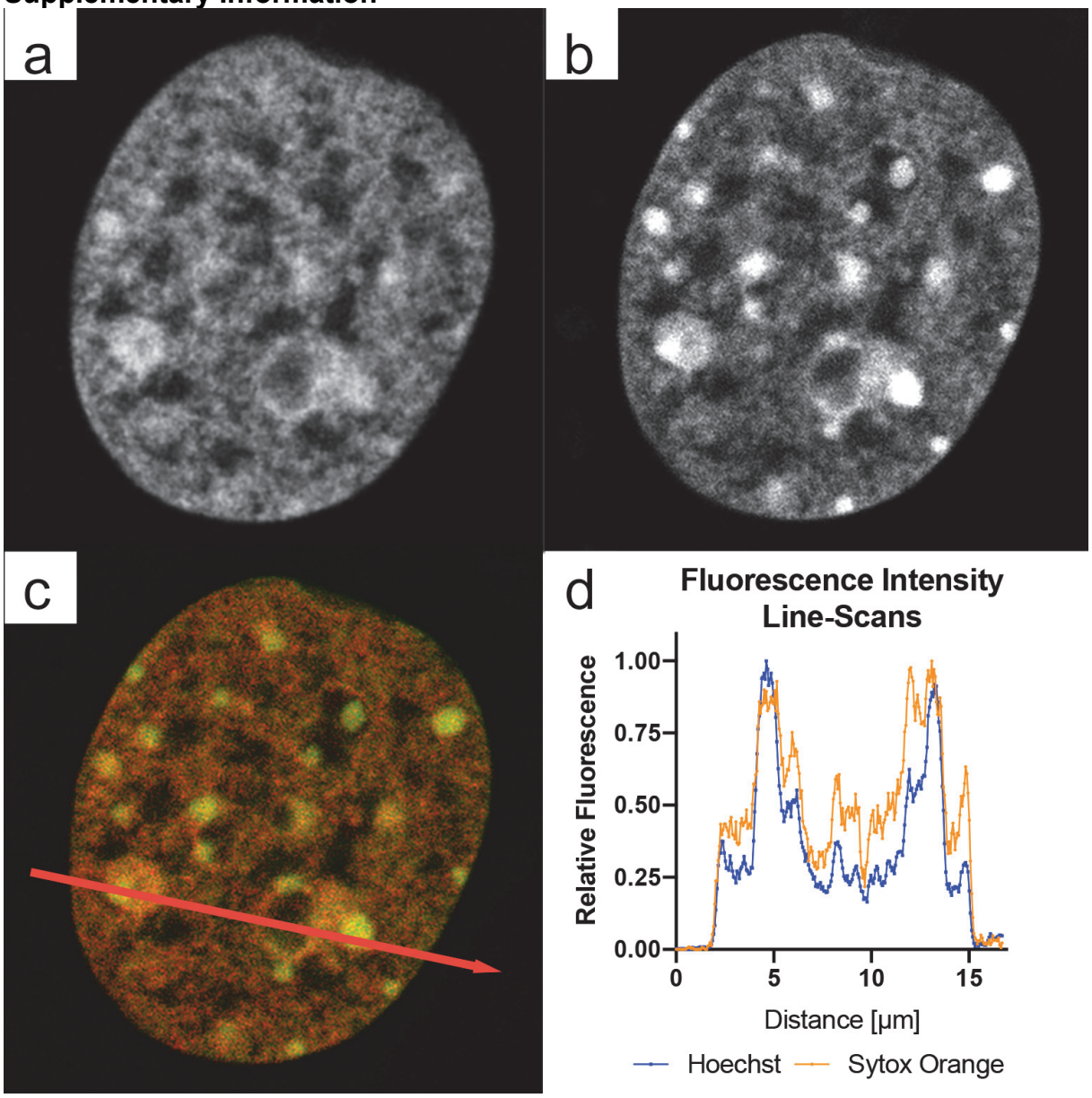

935
936 **Supplemental Figure S1**
937 **Comparison of Sytox Orange and Hoechst 33342 DNA counterstains**
938 *Confocal light-optical section of a C3H10T1/2 nucleus after RNase digestion and double-*
939 *staining with the DNA dyes:* ***a*** *Sytox Orange,* ***b*** *Hoechst 33342,* ***c*** *merged image.* ***d***
940 *Fluorescence intensity distribution of both signals along the line through the nucleus shown*
941 *ina-c. Note the improved staining of Sytox Orange in euchromatic regions.*

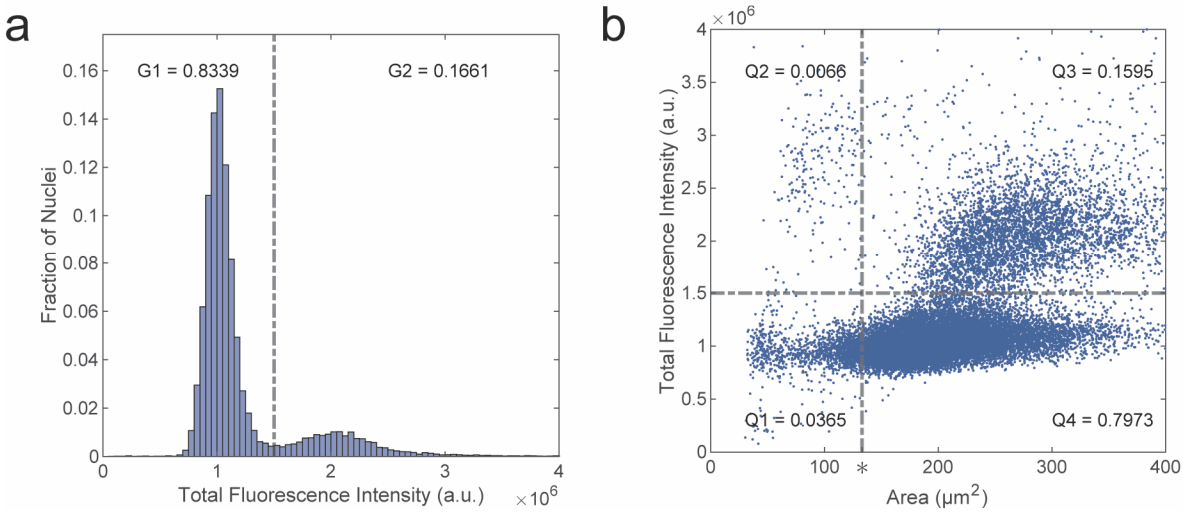

Supplemental Figure S2

Cell cycle estimation of BJ1 nuclei

a *Histogram of total fluorescence intensities of BJ1 nuclei stained with Sytox Orange. For an estimate of the cell cycle stage, cell nuclei with a total fluorescence intensity below or equal to 1.5 x 10^6 a.u. (arbitrary units) were attributed to G1, and nuclei above this threshold were attributed to G2. According to this, 83 percent of the cells were found in G1 and 17 % in G2.* ***b*** *Total fluorescence intensity plotted vs nuclear area. The horizontal dashed line denotes the total fluorescence intensity that was used to discriminate G1 and G2 in (a). The vertical dashed line indicates the size of the BJ1 cell shown in Fig. 2. Q1 to Q4 give the fraction of nuclei found in the 4 quadrants.*

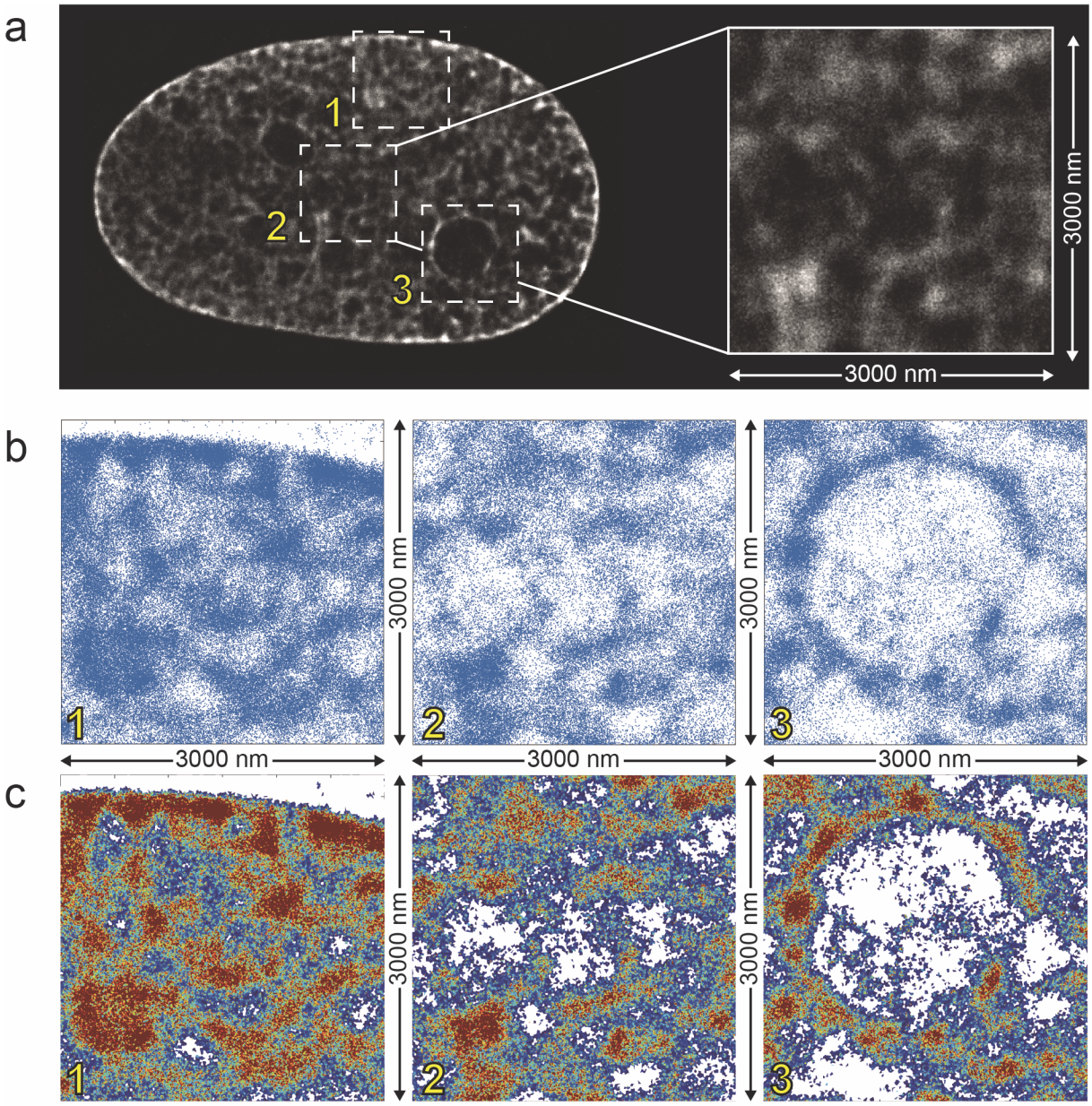

Supplemental Figure S3

Processing of SMLM images and generation of high-resolution nuclear landscapes

a *SMLM-fBALM image of a mid-plane optical section through a BJ1 cell nucleus stained with Sytox Orange yielding about 10 million SMPs with a lateral structural resolution of about 20 nm and an axial resolution of about 600 nm. SMPs were binned in pixels with 10 nm edge length. For this overview, a region was chosen with densely arranged SMPs corresponding to the INC. The three boxes mark regions at the nuclear periphery (1), in the nuclear center (2) and a nucleolus (3). Supplemental Video S1a shows a movie of the enlarged box 2 in (a) with SMPs at increasing density and structural resolution; Supplemental Video S1b provides a view on the rotating 600 nm thick section.* ***b, 1-3*** *Enlargements of boxes 1-3 represent 2D localization maps of all individual SMPs in 100 nm thick optical subsections with an average lateral localization precision of ca. 8 nm and ca. 50 nm along the optical axis (see Results for explanation, how 100 nm thick subsections were achieved from the 600 nm thick primary optical section).* ***c, 1-3*** *The same boxes as above are presented here after Voronoi-tessellation as true-to-scale color-coded DNA density maps (Mbp/µm^3); compare DNA density scale bar in Figure 2, where the identical panel is shown in Fig. 2b1-3. For calculations of 3D DNA densities see Results.*

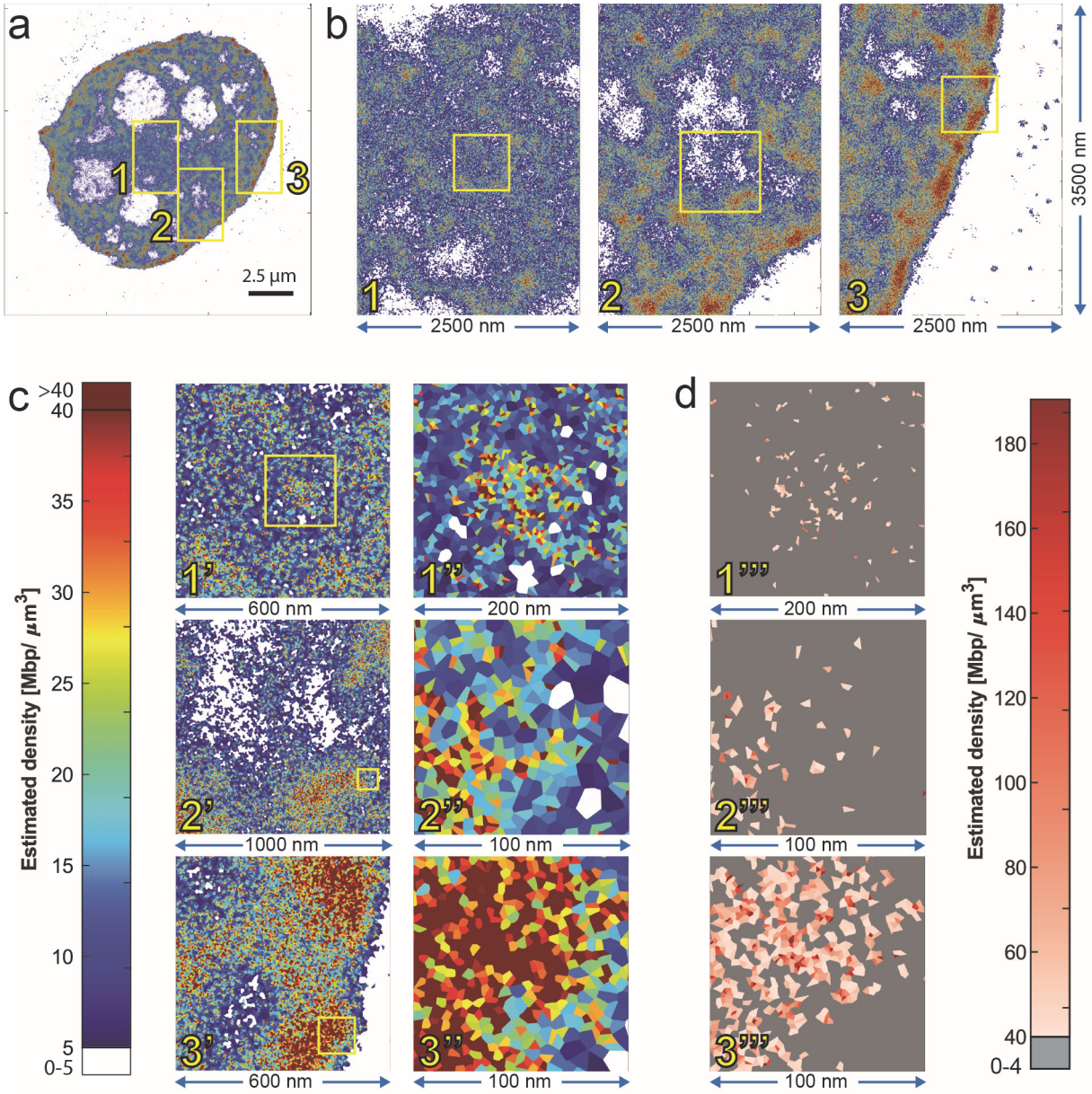

Supplemental Figure S4

High-resolution, true-to-scale DNA density landscape of another HeLa cell nucleus.

a *Voronoi-tessellated SMLM-fBALM image from a mid-optical section through another HeLa cell nucleus shown for a phenotypic comparison with the nucleus in Fig.3. b, 1-3 Magnifications of the three boxed areas in (a); edge lengths 2.5 µm x 3.5 µm.* ***c*** *color map, indicating 0-5 Mbp/µm³ (white), and the range from 5 to (dark blue) to >40 Mbp/µm³ (dark red) (as described in Figure 2).* ***c, 1'-3'*** *Further magnification of boxed areas in (b,1-3); edge length 600 nm(1'), 1 µm (2'), and 600 nm (3').* ***c, 1''-3''*** *Further magnification of boxed areas in c,1'- 3'; edge length 200 nm (1'') and 100 nm in (2'') and (3'').* ***d, 1'''- 3'''*** *presents the same regions as in c,1''- 3'' using another color code (also described in Figure 2), demonstrating the range of apparent DNA densities above 40 Mbp/µm³ up (light red) up to maximum densities of ~180 Mbp/µm³ (dark red), whereas all Voronoi areas assigned to densities between 0 and 40 Mbp/µm³ are grey colored. Note: Image recording of this nucleus was performed without an astigmatic lens, yielding a thickness of the optical section of about 600 nm. Within this optical section, about 4 million blinking DNA-bound Sytox Orange molecules were registered in 25,000 consecutive frames. The midsection of the nucleus presented in Figure 3 is smaller (88 µm²) than the midsection area of this nucleus (96 µm²), which arguably may reflect a DNA density landscape of a transcriptionally more active cell nucleus.*

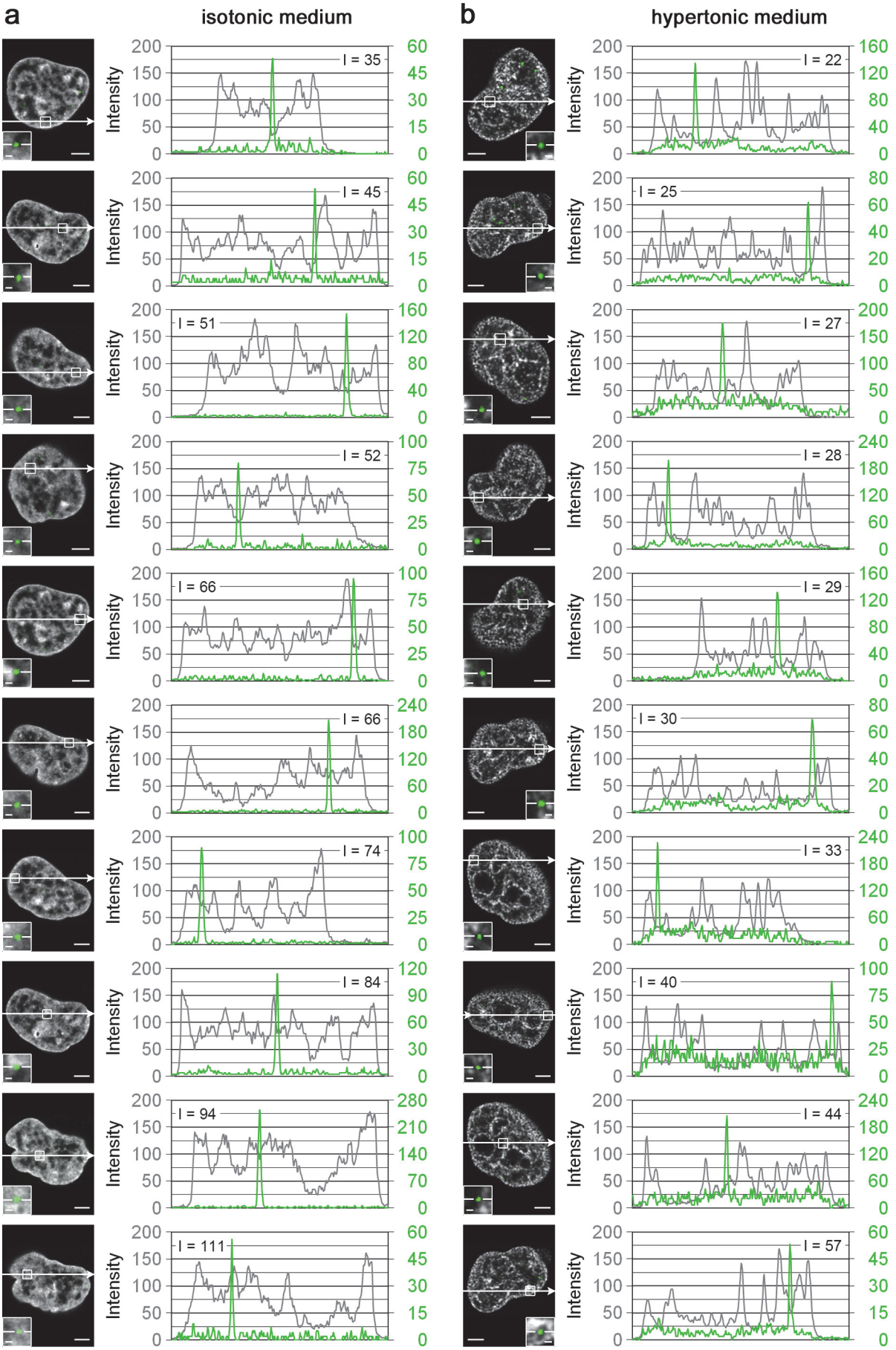
a
isotonic medium
b
hypertonic medium
Intensity
I = 35
I = 45
I = 51
I = 52
I = 66
I = 66
I = 74
I = 84
I = 94
I = 111
I = 22
I = 25
I = 27
I = 28
I = 29
I = 30
I = 33
I = 40
I = 44
I = 57

993
994

995 **Supplemental Figure S5**
996 **Localization of microinjected 20 nm nanobeads**
997 *Localization of nanobeads (with 20 nm diameter) in nuclei of HeLa cells kept in* ***(a)*** *isotonic*
998 *medium with normally condensed chromatin (NCC) or* ***(b)*** *hypertonic medium with hyper-*
999 *condensed chromatin (HCC). The confocal sections (left columns in a and b) show the position*
1000 *of the intensity line plotted at the right; the arrow denotes the scanning direction. The area of*
1001 *the bead is magnified in the inset. Scale bars: 4 µm, 0.5 µm in insets. For each nucleus, line*
1002 *scans were made through a given bead (green line) and through the normalized DAPI intensity*
1003 *image (black line). The relative DNA density (I; grey values 0 - 255) present at the site of a*
1004 *nanobead was determined in the confocal section with the brightest spot. Nanobeads are*
1005 *localized within valleys of the DNA density landscape and sometimes at the slope of DNA*
1006 *density peaks.*

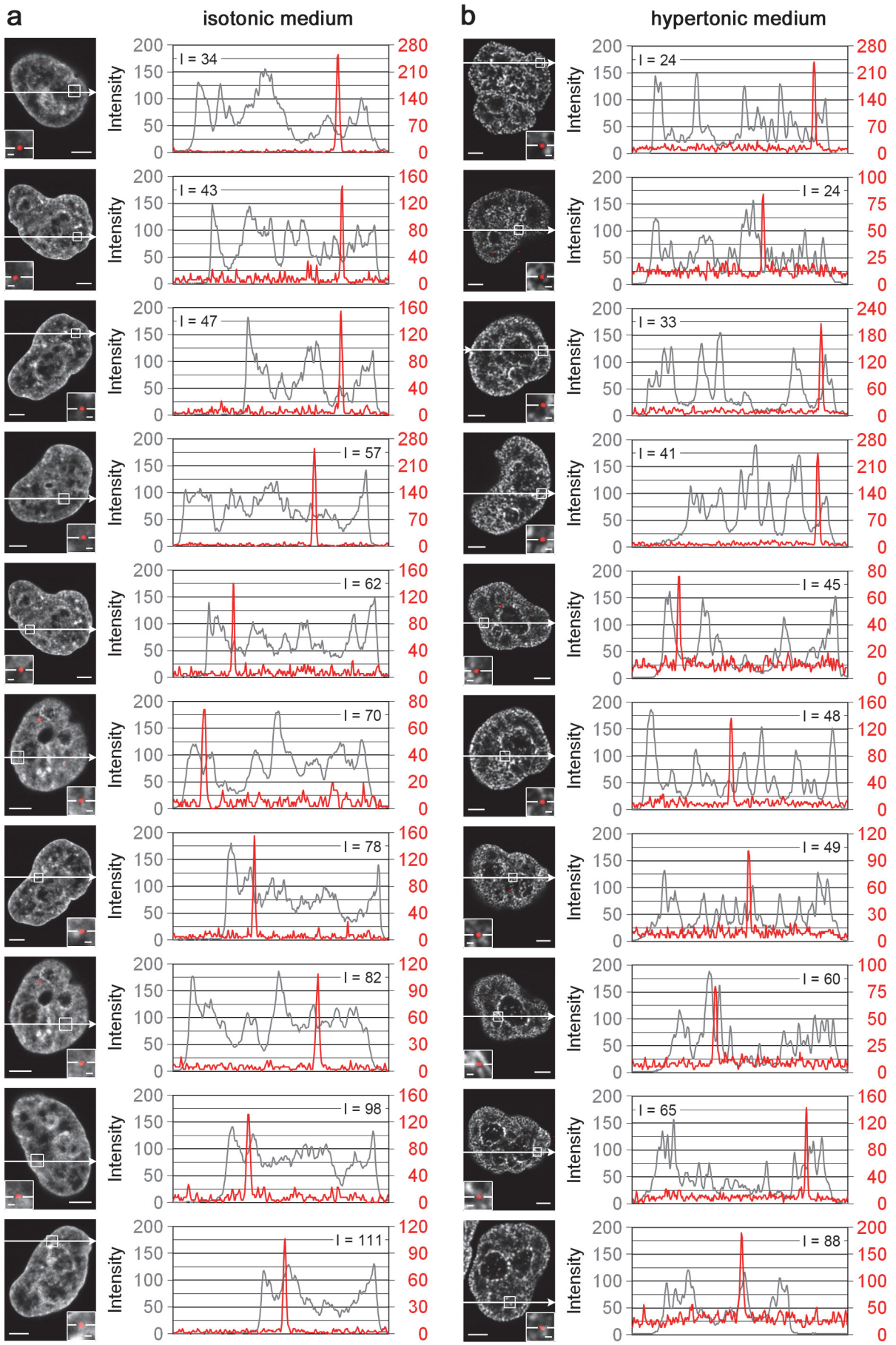
a
isotonic medium
b
hypertonic medium
Intensity
I = 34
I = 43
I = 47
I = 57
I = 62
I = 70
I = 78
I = 82
I = 98
I = 111
I = 24
I = 24
I = 33
I = 41
I = 45
I = 48
I = 49
I = 60
I = 65
I = 88

1007
1008

1009 **Supplemental Figure S6**
1010 **Localization of microinjected 40 nm nanobeads**
1011 *Localization of nanobeads (with 40 nm diameter) in nuclei of HeLa cells kept* ***(a)*** *in isotonic*
1012 *medium with normally condensed chromatin (NCC) or* ***(b)*** *hypertonic medium with hyper-*
1013 *condensed chromatin (HCC). Nanobeads are localized within valleys of the DNA density*
1014 *landscape and sometimes at the slope of DNA density peaks. For further details see legend*
1015 *to Supplemental Figure S5.*
1016

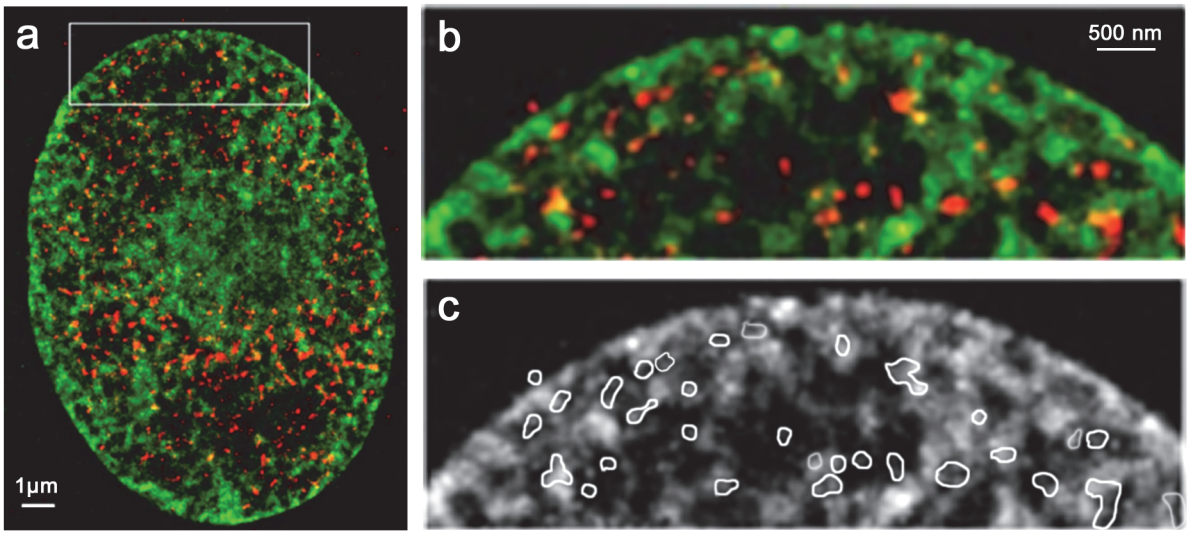

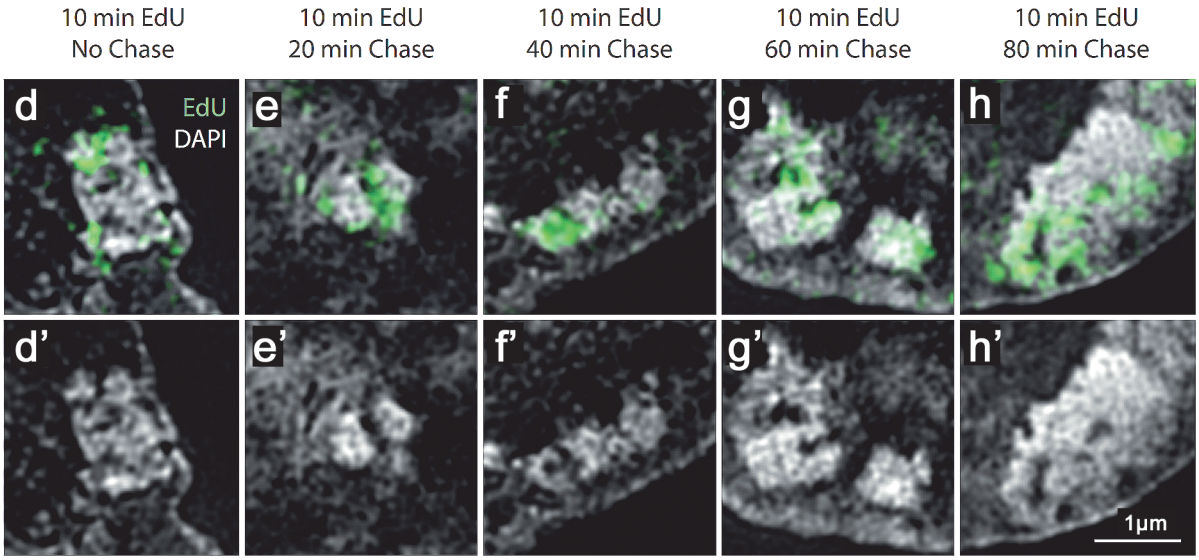

1017
1018 **Supplemental Figure S7**
1019 **Evidence for DNA replication within the ANC and subsequent relocation of**
1020 **replicated DNA into the INC of heterochromatin blocks.**
1021 ***a-c*** *Replication domains (RDs, red) in a HeLa cell nucleus at early S-phase, recorded with*
1022 *SMLM. The cell was fixed immediately after a 15 min pulse-labeling with the thymidine DNA*
1023 *base analog EdU, coupled with Alexa Fluor 555. The nuclear section demonstrates the location*
1024 *of RDs with newly replicated DNA (red) in the ANC, in particular on the surface of chromatin*
1025 *clusters (DNA stained with Vybrant Violet, green).* ***a*** *Dual color SMLM image of the entire*
1026 *nuclear section.* ***b-c*** *Magnification of boxed area shown in (a).* ***c*** *White outlines demonstrate*
1027 *the location of most EdU-labeled RDs at the periphery of chromatin domains (white-grey),*
1028 *expanding in section areas (black) attributed to the interchromatin compartment (IC).* ***d-h*** *EdU-*

1029 *pulse-chase experiment of heterochromatic blocks in undifferentiated mouse embryonic stem*
1030 *cells in mid-late S-phase, recorded with SIM. Optical sections show an overlay of DAPI stained*
1031 *DNA (white-gray) and replicated DNA after application of a 10min pulse with EdU (coupled to*
1032 *Alexa488; green).* ***d*** *Cell fixed immediately after the EdU-pulse demonstrates replicated DNA*
1033 *located mostly within low density DNA of wide IC-channels (attributed to the ANC).* ***e-h*** *cells*
1034 *fixed after increasing chase-time of 20/40/60/80 min before fixation show a relocation of*
1035 *labeled DNA into dense DNA of heterochromatic blocks (attributed to the INC).* ***d'-h'*** *DAPI*
1036 *stained DNA only. This result provides a glimpse into the dynamics of chromatin movements*
1037 *between immediately adjacent ANC and INC compartments.*
1038

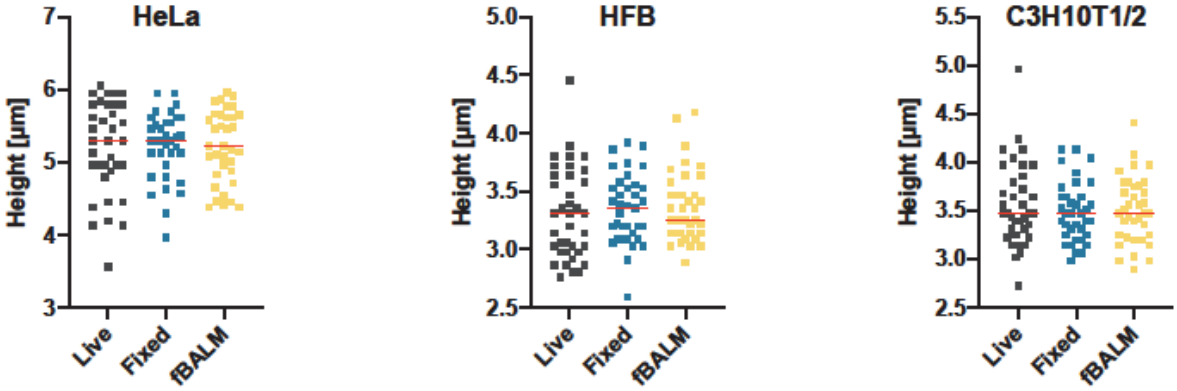

1039
1040 **Supplemental Figure S8**
1041 **Measurements of cell-heights in live-cells, fixed cells in 1x dPBS and in fBALM**
1042 **imaging buffer.**
1043 *To test, whether cell fixation and high-resolution imaging with SMLM-fBALM has a flattening*
1044 *effect on nuclear morphology, we determined the height of HeLa nuclei (**a**), C3H10T1/2 (**b**)*
1045 *nuclei and HFB nuclei (**c**) in living and fixed cells, as well as in cells kept in fBALM imaging*
1046 *buffer. 20 min after adding Hoechst 33342, z-stacks with 200 nm intervals were recorded on a*
1047 *Visitron Spinning Disk microscope equipped with a 405 nm diode laser and a Photometrics*
1048 *Prime BSI camera using a 60x Nikon water immersion objective lens NA 1.2 attached to a*
1049 *Nikon Ti2 Microscopic stand. Nuclear heights were measured in image stacks with ImageJ in*
1050 *the x,y or y,z view. Red lines indicate the mean. Note that nuclear heights were not corrected*
1051 *for the limited depth resolution of the objective lens. Since this bias was the same for all*
1052 *recorded cells, it did not affect the comparative measurements. Conclusion: For each cell*
1053 *type, the nuclear heights were not significantly affected in living and fixed cells with or without*
1054 *incubation with fBALM buffer: HeLa (N=35, ANOVA P=0.98), HFb (N=37, ANOVA*
1055 *P=0.73) and C3H10T1/2 (N=36, ANOVA P=0.65).*
1056
1057 **Supplemental Videos S1a and S1b**
1058 *Movie with the positions of blinking signals (SMPs) recorded from DNA bound Sytox Orange*
1059 *molecules (SMPs) in the BJ1 nucleus shown in Figure 2. The SM positions of a mid-plane*
1060 *optical section (thickness ~ 600 nm) of this BJ1-nucleus with about 10 million localizations*
1061 *were visualized by assigning each SM position to a 10 nm sized pixel (corresponding to the*
1062 *average localization precision of 8.5 nm).* ***Video S1a*** *starts with the visualization of the entire*
1063 *nuclear section and then zooms in to smaller regions of interest (boxed area 2).* ***Video S1b***
1064 *provides a view on the rotating 600 nm thick section.*
1065
1066 **Supplemental Video S2**
1067 *Movie of a C3H 10T1/2 nucleus recorded for 6 hours after microinjection of three 20 nm sized*
1068 *nanobeads. Magnified images of two nanobeads in the 'lower' part of the nucleus are shown*
1069 *in Figure 5f,g. Other nanobeads or clusters were located in the cytoplasm, as demonstrated*
1070 *by serial sections. The display on the left shows the moving, intranuclear nanobeads. Notably,*

movements of nanobeads in the cytoplasm were more rapid and extensive. The right display demonstrates a random-walk like trajectories of intranuclear nanobeads (compare Figure 5h).

References

Albiez, H., Cremer, M., Tiberi, C., Vecchio, L., Schermelleh, L., Dittrich, S., Kupper, K., Joffe, B., Thormeyer, T., von Hase, J.*, et al.* (2006). Chromatin domains and the interchromatin compartment form structurally defined and functionally interacting nuclear networks. Chromosome Res *14*, 707-733.

Amiad-Pavlov, D., Lorber, D., Bajpai, G., Reuveny, A., Roncato, F., Alon, R., Safran, S., and Volk, T. (2021). Live imaging of chromatin distribution reveals novel principles of nuclear architecture and chromatin compartmentalization. Sci Adv *7*.

Amitai, A., and Holcman, D. (2017). Polymer physics of nuclear organization and function. Physics Reports *678*, 1-83.

Andronov, L., Orlov, I., Lutz, Y., Vonesch, J.L., and Klaholz, B.P. (2016). ClusterViSu, a method for clustering of protein complexes by Voronoi tessellation in super-resolution microscopy. Sci Rep *6*, 24084.

Babokhov, M., Hibino, K., Itoh, Y., and Maeshima, K. (2020). Local Chromatin Motion and Transcription. J Mol Biol *432*, 694-700.

Bairstow, F., and Heidelberger, C. (1975). Increased thymidine uptake by methylcholanthrene-treated C3H/10T1/2 cells. Int J Cancer *16*, 370-375.

Bajpai, G., Amiad Pavlov, D., Lorber, D., Volk, T., and Safran, S. (2021). Mesoscale phase separation of chromatin in the nucleus. Elife *10*.

Baldi, S., Korber, P., and Becker, P.B. (2020). Beads on a string-nucleosome array arrangements and folding of the chromatin fiber. Nat Struct Mol Biol *27*, 109-118.

Barth, R., Bystricky, K., and Shaban, H.A. (2020). Coupling chromatin structure and dynamics by live super-resolution imaging. Sci Adv *6*.

Bascom, G.D., Myers, C.G., and Schlick, T. (2019). Mesoscale modeling reveals formation of an epigenetically driven HOXC gene hub. Proc Natl Acad Sci U S A *116*, 4955-4962.

Bascom, G.D., Sanbonmatsu, K.Y., and Schlick, T. (2016). Mesoscale Modeling Reveals Hierarchical Looping of Chromatin Fibers Near Gene Regulatory Elements. J Phys Chem B *120*, 8642-8653.

Beagrie, R.A., Thieme, C.J., Annunziatella, C., Baugher, C., Zhang, Y., Schueler, M., Kramer, D.C.A., Chiarello, A.M., Bianco, S., Kukalev, A.*, et al.* (2021). Multiplex-GAM: genome-wide identification of chromatin contacts yields insights not captured by Hi-C bioRxiv.

Belmont, A.S. (2021). Nuclear Compartments: An Incomplete Primer to Nuclear Compartments, Bodies, and Genome Organization Relative to Nuclear Architecture. Cold Spring Harb Perspect Biol.

Bintu, B., Mateo, L.J., Su, J.H., Sinnott-Armstrong, N.A., Parker, M., Kinrot, S., Yamaya, K., Boettiger, A.N., and Zhuang, X. (2018). Super-resolution chromatin tracing reveals domains and cooperative interactions in single cells. Science *362*.

Branco, M.R., and Pombo, A. (2006). Intermingling of chromosome territories in interphase suggests role in translocations and transcription-dependent associations. PLoS Biol *4*, e138.

Cai, L., Panyukov, s., and Rubinstein, M. (2015). Hopping Diffusion of Nanoparticles in Polymer Matrices. Macromolecules *48*, 847-862.

Cardozo Gizzi, A.M. (2021). A Shift in Paradigms: Spatial Genomics Approaches to Reveal Single-Cell Principles of Genome Organization. Front Genet *Article 780822*.

Chen, S.-Y., Bestvater, F., Schaufler, W., Heintzmann, R., and Cremer, C. (2018). Patterned illumination single molecule localization microscopy (piSMLM): user defined blinking regions of interest. Opt Express *26*, 30009-30020.

Chen, S.Y. (2020). Advanced Single Molecule Localization Microscopy for imaging cellular nuclei. . PhD Thesis, University Jena.

Chen, S.Y., Heintzmann, R., and Cremer, C. (2019). Sample drift estimation method based on speckle patterns formed by backscattered laser light. Biomed Opt Express *10*, 6462-6475.

Chiariello, A.M., Annunziatella, C., Bianco, S., Esposito, A., and Nicodemi, M. (2016). Polymer physics of chromosome large-scale 3D organisation. Sci Rep *6*, 29775.

1128 Chu, L.A., Chang, S.W., Tang, W.C., Tseng, Y.T., Chen, P., and Chen, B.C. (2021). 5D
1129 superresolution imaging for a live cell nucleus. Curr Opin Genet Dev *67*, 77-83.
1130 Cremer, C., and Masters, B.R. (2013). Resolution enhancement techniques in microscopy. The
1131 European Physical Journal H *38*, 281-344.
1132 Cremer, C., Szczurek, A., Schock, F., Gourram, A., and Birk, U. (2017). Super-resolution
1133 microscopy approaches to nuclear nanostructure imaging. Methods *123*, 11-32.
1134 Cremer, M., Brandstetter, K., Maiser, A., Rao, S.S.P., Schmid, V.J., Guirao-Ortiz, M., Mitra, N.,
1135 Mamberti, S., Klein, K.N., Gilbert, D.M.*, et al.* (2020b). Cohesin depleted cells rebuild
1136 functional nuclear compartments after endomitosis. Nat Commun *11*, 6146.
1137 Cremer, M., and Cremer, T. (2019). Nuclear compartmentalization, dynamics, and function of
1138 regulatory DNA sequences. Genes Chromosomes Cancer *58*, 427-436.
1139 Cremer, M., Kupper, K., Wagler, B., Wizelman, L., von Hase, J., Weiland, Y., Kreja, L., Diebold,
1140 J., Speicher, M.R., and Cremer, T. (2003). Inheritance of gene density-related higher order
1141 chromatin arrangements in normal and tumor cell nuclei. J Cell Biol *162*, 809-820.
1142 Cremer, T., and Cremer, M. (2010). Chromosome territories. Cold Spring Harb Perspect Biol *2*,
1143 a003889.
1144 Cremer, T., Cremer, M., and Cremer, C. (2018). The 4D Nucleome: Genome
1145 Compartmentalization in an Evolutionary Context. Biochemistry (Mosc) *83*, 313-325.
1146 Cremer, T., Cremer, M., Hubner, B., Silahtaroglu, A., Hendzel, M., Lanctot, C., Strickfaden, H.,
1147 and Cremer, C. (2020a). The Interchromatin Compartment Participates in the Structural
1148 and Functional Organization of the Cell Nucleus. Bioessays *42*, e1900132.
1149 Cremer, T., Cremer, M., Hubner, B., Strickfaden, H., Smeets, D., Popken, J., Sterr, M., Markaki,
1150 Y., Rippe, K., and Cremer, C. (2015). The 4D nucleome: Evidence for a dynamic nuclear
1151 landscape based on co-aligned active and inactive nuclear compartments. FEBS Lett *589*,
1152 2931-2943.
1153 Cremer, T., Kreth, G., Koester, H., Fink, R.H.A., Heintzmann, R., Cremer, M., Solovei, I., Zink,
1154 D., and Cremer, C. (2000). Chromosome Territories, Interchromatin Domain Compartment,
1155 and Nuclear Matrix: An Integrated View of the Functional Nuclear Architecture. Critical
1156 reviews in Eukaryotic Gene Expression 10: 179-212 *10*, 179-212.
1157 Dekker, J., Belmont, A.S., Guttman, M., Leshyk, V.O., Lis, J.T., Lomvardas, S., Mirny, L.A.,
1158 O'Shea, C.C., Park, P.J., Ren, B.*, et al.* (2017). The 4D nucleome project. Nature *549*, 219-
1159 226.
1160 Di Stefano, M., Paulsen, J., Lien, T.G., Hovig, E., and Micheletti, C. (2016). Hi-C-constrained
1161 physical models of human chromosomes recover functionally-related properties of
1162 genome organization. Sci Rep *6*, 35985.
1163 Eltsov, M., Maclellan, K.M., Maeshima, K., Frangakis, A.S., and Dubochet, J. (2008). Analysis of
1164 cryo-electron microscopy images does not support the existence of 30-nm chromatin fibers
1165 in mitotic chromosomes in situ. Proc Natl Acad Sci U S A *105*, 19732-19737.
1166 Farabella, I., Di Stefano, M., Soler-Vila, P., Marti-Marimon, M., and Marti-Renom, M.A. (2021).
1167 Three-dimensional genome organization via triplex-forming RNAs. Nat Struct Mol Biol *28*,
1168 945-954.
1169 Finn, E.H., and Misteli, T. (2019). Molecular basis and biological function of variability in spatial
1170 genome organization. Science *365*.
1171 Gasser, S.M., and Laemmli, U. (1987). A glimpse at chromosomal order. Trends in Genetics *3*,
1172 16-22.
1173 Gorisch, S.M., Richter, K., Scheuermann, M.O., Herrmann, H., and Lichter, P. (2003). Diffusion-
1174 limited compartmentalization of mammalian cell nuclei assessed by microinjected
1175 macromolecules. Exp Cell Res *289*, 282-294.
1176 Gorkin, D.U., Barozzi, I., Zhao, Y., Zhang, Y., Huang, H., Lee, A.Y., Li, B., Chiou, J., Wildberg, A.,
1177 Ding, B.*, et al.* (2020). An atlas of dynamic chromatin landscapes in mouse fetal
1178 development. Nature *583*, 744-751.
1179 Gould, T.J., and Bewersdorf, J. (2012). Nanoscopy at low light intensities shows its potential.
1180 Elife *1*, e00475.
1181 Hansen, J.C., Maeshima, K., and Hendzel, M.J. (2021). The solid and liquid states of chromatin.
1182 Epigenetics Chromatin *14*, 50.
1183 Hell, S., and Stelzer, E.H.K. (1992). Properties of a 4Pi confocal fluorescence microscope. J Opt
1184 Soc Am A *9*, 2159-2166.

1185 Hendzel, M.J., and Bazett-Jones, D.P. (1996). Probing nuclear ultrastructure by electron
1186 spectroscopic imaging. J Microsc *182*, 1-14.
1187 Huang, B., Wang, W., Bates, M., and Zhuang, X. (2008). Three-dimensional super-resolution
1188 imaging by stochastic optical reconstruction microscopy. Science *319*, 810-813.
1189 Hübner, B. (2020). Functional nuclear architecture in normal cells and after manipulation of
1190 the nuclear landscape. Dissertation, LMU München: Faculty of Biology Thesis, (Dissertation,
1191 LMU Munich).
1192 Imai, R., Nozaki, T., Tani, T., Kaizu, K., Hibino, K., Ide, S., Tamura, S., Takahashi, K., Shribak, M.,
1193 and Maeshima, K. (2017). Density imaging of heterochromatin in live cells using
1194 orientation-independent-DIC microscopy. Mol Biol Cell *28*, 3349-3359.
1195 Jerkovic, I., and Cavalli, G. (2021). Understanding 3D genome organization by multidisciplinary
1196 methods. Nat Rev Mol Cell Biol *22*, 511-528.
1197 Kaufmann, R., Lemmer, P., Gunkel, M., Weiland, Y., Müller, P., Hausmann, M., Baddeley, D.,
1198 Amberger, R., and Cremer, C. (2009). SPDM: single molecule superresolution of cellular
1199 nanostructures, Vol 7185 (SPIE).
1200 Kempfer, R., and Pombo, A. (2020). Methods for mapping 3D chromosome architecture. Nat
1201 Rev Genet *21*, 207-226.
1202 Kharerin, H., Bhat, P.J., and Padinhateeri, R. (2020). Role of nucleosome positioning in 3D
1203 chromatin organization and loop formation. J Biosci *45*.
1204 Khater, I.M., Nabi, I.R., and Hamarneh, G. (2020). A Review of Super-Resolution Single-
1205 Molecule Localization Microscopy Cluster Analysis and Quantification Methods. Patterns
1206 (N Y) *1*, 100038.
1207 Kirmes, I., Szczurek, A., Prakash, K., Charapitsa, I., Heiser, C., Musheev, M., Schock, F.,
1208 Fornalczyk, K., Ma, D., Birk, U*., et al.* (2015). A transient ischemic environment induces
1209 reversible compaction of chromatin. Genome Biol *16*, 246.
1210 Landry, J.J., Pyl, P.T., Rausch, T., Zichner, T., Tekkedil, M.M., Stutz, A.M., Jauch, A., Aiyar, R.S.,
1211 Pau, G., Delhomme, N*., et al.* (2013). The genomic and transcriptomic landscape of a HeLa
1212 cell line. G3 (Bethesda) *3*, 1213-1224.
1213 Lang, F., Contreras-Gerenas, M.F., Gelleri, M., Neumann, J., Kroger, O., Sadlo, F., Berniak, K.,
1214 Marx, A., Cremer, C., Wagenknecht, H.A*., et al.* (2021). Tackling Tumour Cell Heterogeneity
1215 at the Super-Resolution Level in Human Colorectal Cancer Tissue. Cancers (Basel) *13*.
1216 Leidescher, S., Ribisel, J., Ulrich, S., Feodorova, Y., Hildebrand, E., Galitsyna, A., Bultmann, S.,
1217 Link, S., Thanisch, K., Mulholland, C*., et al.* (2022). Spatial organization of transcribed
1218 eukaryotic genes. Nature Cell Biology *in pres*.
1219 Lelek, M., Gyparaki, M.T., Beliu, G., Schueder, F., Griffie, J., Manley, S., Jungmann, R., Sauer,
1220 M., Lakadamyali, M., and Zimmer, C. (2021). Single-molecule localization microscopy. Nat
1221 Rev Methods Primers *1*.
1222 Lenart, P., Rabut, G., Daigle, N., Hand, A.R., Terasaki, M., and Ellenberg, J. (2003). Nuclear
1223 envelope breakdown in starfish oocytes proceeds by partial NPC disassembly followed by
1224 a rapidly spreading fenestration of nuclear membranes. J Cell Biol *160*, 1055-1068.
1225 Levet, F., Hosy, E., Kechkar, A., Butler, C., Beghin, A., Choquet, D., and Sibarita, J.B. (2015). SR-
1226 Tesseler: a method to segment and quantify localization-based super-resolution
1227 microscopy data. Nat Methods *12*, 1065-1071.
1228 Lieberman-Aiden, E., van Berkum, N.L., Williams, L., Imakaev, M., Ragoczy, T., Telling, A., Amit,
1229 I., Lajoie, B.R., Sabo, P.J., Dorschner, M.O*., et al.* (2009). Comprehensive mapping of long-
1230 range interactions reveals folding principles of the human genome. Science *326*, 289-293.
1231 Lohoff, T., Ghazanfar, S., Missarova, A., Koulena, N., Pierson, N., Griffiths, J.A., Bardot, E.S.,
1232 Eng, C.L., Tyser, R.C.V., Argelaguet, R*., et al.* (2022). Integration of spatial and single-cell
1233 transcriptomic data elucidates mouse organogenesis. Nat Biotechnol *40*, 74-85.
1234 Ma, H., Tu, L.C., Naseri, A., Huisman, M., Zhang, S., Grunwald, D., and Pederson, T. (2016).
1235 CRISPR-Cas9 nuclear dynamics and target recognition in living cells. J Cell Biol *214*, 529-537.
1236 Maeshima, K., Kaizu, K., Tamura, S., Nozaki, T., Kokubo, T., and Takahashi, K. (2015). The
1237 physical size of transcription factors is key to transcriptional regulation in chromatin
1238 domains. J Phys Condens Matter *27*, 064116.
1239 Markaki, Y., Smeets, D., Cremer, M., and Schermelleh, L. (2013). Fluorescence in situ
1240 hybridization applications for super-resolution 3D structured illumination microscopy.
1241 Methods Mol Biol *950*, 43-64.

Maslova, A., and Krasikova, A. (2021). FISH Going Meso-Scale: A Microscopic Search for Chromatin Domains. Front Cell Dev Biol *9*, 753097.
Meggendorfer, M., Weierich, C., Wolff, H., Brack-Werner, R., and Cremer, T. (2010). Functional nuclear topography of transcriptionally inducible extra-chromosomal transgene clusters. Chromosome Res *18*, 401-417.
Minnoye, L., Marinaov, G.K., Krausgruber, T., Pan, L., Marand, A.P., Secchia, S., Greenleaf, W.J., Furlong, E.E.M., Zhao, K., Schmitz, R.J.*, et al.* (2021). Chromatin accessibility profiling methods. Nature Reviews Methods Primers *1*.
Miron, E., Oldenkamp, R., Brown, J.M., Pinto, D.M.S., Xu, C.S., Faria, A.R., Shaban, H.A., Rhodes, J.D.P., Innocent, C., de Ornellas, S.*, et al.* (2020). Chromatin arranges in chains of mesoscale domains with nanoscale functional topography independent of cohesin. Science Advances *6*, eaba8811.
Misteli, T. (2020). The Self-Organizing Genome: Principles of Genome Architecture and Function. Cell *183*, 28-45.
Moretti, C., Stevant, I., and Ghavi-Helm, Y. (2020). 3D genome organisation in Drosophila. Brief Funct Genomics *19*, 92-100.
Nagano, T., Lubling, Y., Varnai, C., Dudley, C., Leung, W., Baran, Y., Mendelson Cohen, N., Wingett, S., Fraser, P., and Tanay, A. (2017). Cell-cycle dynamics of chromosomal organization at single-cell resolution. Nature *547*, 61-67.
Neguembor, M.V., Martin, L., Castells-Garcia, A., Gomez-Garcia, P.A., Vicario, C., Carnevali, D., AlHaj Abed, J., Granados, A., Sebastian-Perez, R., Sottile, F.*, et al.* (2021). Transcription-mediated supercoiling regulates genome folding and loop formation. Mol Cell *81*, 3065-3081 e3012.
Nguyen, H.Q., Chattoraj, S., Castillo, D., Nguyen, S.C., Nir, G., Lioutas, A., Hershberg, E.A., Martins, N.M.C., Reginato, P.L., Hannan, M.*, et al.* (2020). 3D mapping and accelerated super-resolution imaging of the human genome using in situ sequencing. Nat Methods *17*, 822-832.
Nir, G., Farabella, I., Perez Estrada, C., Ebeling, C.G., Beliveau, B.J., Sasaki, H.M., Lee, S.D., Nguyen, S.C., McCole, R.B., Chattoraj, S.*, et al.* (2018). Walking along chromosomes with super-resolution imaging, contact maps, and integrative modeling. PLoS Genet *14*, e1007872.
Nussinov, R., Jang, H., Nir, G., Tsai, C.J., and Cheng, F. (2021). A new precision medicine initiative at the dawn of exascale computing. Signal Transduct Target Ther *6*, 3.
Odenheimer, J., Heermann, D.W., and Kreth, G. (2009). Brownian dynamics simulations reveal regulatory properties of higher-order chromatin structures. Eur Biophys J *38*, 749-756.
Paulsen, J., Liyakat Ali, T.M., and Collas, P. (2018). Computational 3D genome modeling using Chrom3D. Nat Protoc *13*, 1137-1152.
Pluen, A., Netti, P.A., Jain, R.K., and Berk, D.A. (1999). Diffusion of macromolecules in agarose gels: comparison of linear and globular configurations. Biophys J *77*, 542-552.
Razin, S.V., and Gavrilov, A.A. (2021). Non-coding RNAs in chromatin folding and nuclear organization. Cell Mol Life Sci *78*, 5489-5504.
Reymann, J., Baddeley, D., Gunkel, M., Lemmer, P., Stadter, W., Jegou, T., Rippe, K., Cremer, C., and Birk, U. (2008). High-precision structural analysis of subnuclear complexes in fixed and live cells via spatially modulated illumination (SMI) microscopy. Chromosome Res *16*, 367-382.
Ricci, M.A., Manzo, C., Garcia-Parajo, M.F., Lakadamyali, M., and Cosma, M.P. (2015). Chromatin fibers are formed by heterogeneous groups of nucleosomes in vivo. Cell *160*, 1145-1158.
Rosa, A., and Zimmer, C. (2014). Computational models of large-scale genome architecture. Int Rev Cell Mol Biol *307*, 275-349.
Roukos, V., Pegoraro, G., Voss, T.C., and Misteli, T. (2015). Cell cycle staging of individual cells by fluorescence microscopy. Nat Protoc *10*, 334-348.
Rouquette, J., Cremer, C., Cremer, T., and Fakan, S. (2010). Functional nuclear architecture studied by microscopy: present and future. Int Rev Cell Mol Biol *282*, 1-90.
Rowley, M.J., and Corces, V.G. (2018). Organizational principles of 3D genome architecture. Nat Rev Genet *19*, 789-800.
Schermelleh, L., Ferrand, A., Huser, T., Eggeling, C., Sauer, M., Biehlmaier, O., and Drummen, G.P.C. (2019). Super-resolution microscopy demystified. Nat Cell Biol *21*, 72-84.

Schmid, V.J., Cremer, M., and Cremer, T. (2017). Quantitative analyses of the 3D nuclear landscape recorded with super-resolved fluorescence microscopy. Methods *123*, 33-46.
Seelbinder, B., Jain, M., Erben, E., Klykov, S., Stoev, I.D., and Kreysing, M. (2021). Non-invasive Chromatin Deformation and Measurement of Differential

Mechanical Properties in the Nucleus. BioRxiv preprint.
Shechtman, Y., Gustavsson, A.K., Petrov, P.N., Dultz, E., Lee, M.Y., Weis, K., and Moerner, W.E. (2017). Observation of live chromatin dynamics in cells via 3D localization microscopy using Tetrapod point spread functions. Biomed Opt Express *8*, 5735-5748.
Simakov, O., Bredeson, J., Berkoff, K., Marletaz, F., Mitros, T., Schultz, D.T., O'Connell, B.L., Dear, P., Martinez, D.E., Steele, R.E.*, et al.* (2022). Deeply conserved synteny and the evolution of metazoan chromosomes. Sci Adv *8*, eabi5884.
Smeets, D., Markaki, Y., Schmid, V.J., Kraus, F., Tattermusch, A., Cerase, A., Sterr, M., Fiedler, S., Demmerle, J., Popken, J.*, et al.* (2014). Three-dimensional super-resolution microscopy of the inactive X chromosome territory reveals a collapse of its active nuclear compartment harboring distinct Xist RNA foci. Epigenetics Chromatin *7*, 8.
Snyder, M.P., Lin, S., Posgai, A., Atkinson, M., Regev, A., Rood, J., Rozenblatt-Rosen, O., Gaffney, L., Hupalowska, A., Satija, R.*, et al.* (2019). The human body at cellular resolution: the NIH Human Biomolecular Atlas Program. Nature *574*, 187-192.
Solovei, I., Kienle, D., Little, G., Eils, R., Savelyeva, L., Schwab, M., Jager, W., Cremer, C., and Cremer, T. (2000). Topology of double minutes (dmins) and homogeneously staining regions (HSRs) in nuclei of human neuroblastoma cell lines. Genes Chromosomes Cancer *29*, 297-308.
Strickfaden, H. (2021). Reflections on the organization and the physical state of chromatin in eukaryotic cells. Genome *64*, 311-325.
Strickfaden, H., Tolsma, T.O., Sharma, A., Underhill, D.A., Hansen, J.C., and Hendzel, M.J. (2020). Condensed Chromatin Behaves like a Solid on the Mesoscale In Vitro and in Living Cells. Cell *183*, 1772-1784 e1713.
Strickfaden, H., Xu, Z.Z., and Hendzel, M.J. (2015). Visualization of miniSOG Tagged DNA Repair Proteins in Combination with Electron Spectroscopic Imaging (ESI). J Vis Exp.
Strickfaden, H., Zunhammer, A., van Koningsbruggen, S., Kohler, D., and Cremer, T. (2010). 4D chromatin dynamics in cycling cells: Theodor Boveri's hypotheses revisited. Nucleus *1*, 284-297.
Sureka, R., and Mishra, R. (2021). Identification of Evolutionarily Conserved Nuclear Matrix Proteins and Their Prokaryotic Origins. J Proteome Res *20*, 518-530.
Swygert, S.G., Lin, D., Portillo-Ledesma, S., Lin, P.Y., Hunt, D.R., Kao, C.F., Schlick, T., Noble, W.S., and Tsukiyama, T. (2021). Local chromatin fiber folding represses transcription and loop extrusion in quiescent cells. Elife *10*.
Szabo, Q., Bantignies, F., and Cavalli, G. (2019). Principles of genome folding into topologically associating domains. Sci Adv *5*, eaaw1668.
Szabo, Q., Jost, D., Chang, J.M., Cattoni, D.I., Papadopoulos, G.L., Bonev, B., Sexton, T., Gurgo, J., Jacquier, C., Nollmann, M.*, et al.* (2018). TADs are 3D structural units of higher-order chromosome organization in Drosophila. Sci Adv *4*, eaar8082.
Szczurek, A., Birk, U., Knecht, H., Dobrucki, J., Mai, S., and Cremer, C. (2018). Super-resolution binding activated localization microscopy through reversible change of DNA conformation. Nucleus *9*, 182-189.
Szczurek, A., Klewes, L., Xing, J., Gourram, A., Birk, U., Knecht, H., Dobrucki, J.W., Mai, S., and Cremer, C. (2017). Imaging chromatin nanostructure with binding-activated localization microscopy based on DNA structure fluctuations. Nucleic Acids Res *45*, e56.
Verschure, P.J., van der Kraan, I., Manders, E.M., Hoogstraten, D., Houtsmuller, A.B., and van Driel, R. (2003). Condensed chromatin domains in the mammalian nucleus are accessible to large macromolecules. EMBO Rep *4*, 861-866.
Weidemann, T., Wachsmuth, M., Knoch, T.A., Muller, G., Waldeck, W., and Langowski, J. (2003). Counting nucleosomes in living cells with a combination of fluorescence correlation spectroscopy and confocal imaging. J Mol Biol *334*, 229-240.
Weiland, Y., Lemmer, P., and Cremer, C. (2011). Combining FISH with localisation microscopy: Super-resolution imaging of nuclear genome nanostructures. Chromosome Res *19*, 5-23.
Wolff, H., Hadian, K., Ziegler, M., Weierich, C., Kramer-Hammerle, S., Kleinschmidt, A., Erfle, V., and Brack-Werner, R. (2006). Analysis of the influence of subcellular localization of the

HIV Rev protein on Rev-dependent gene expression by multi-fluorescence live-cell imaging. Exp Cell Res *312*, 443-456.

Wombacher, R., Heidbreder, M., van de Linde, S., Sheetz, M.P., Heilemann, M., Cornish, V.W., and Sauer, M. (2010). Live-cell super-resolution imaging with trimethoprim conjugates. Nat Methods *7*, 717-719.

Xiang, W., Roberti, M.J., Heriche, J.K., Huet, S., Alexander, S., and Ellenberg, J. (2018). Correlative live and super-resolution imaging reveals the dynamic structure of replication domains. J Cell Biol *217*, 1973-1984.

Yang, K.D., Belyaeva, A., Venkatachalapathy, S., Damodaran, K., Katcoff, A., Radhakrishnan, A., Shivashankar, G.V., and Uhler, C. (2021). Multi-domain translation between single-cell imaging and sequencing data using autoencoders. Nat Commun *12*, 31.

Zakirov, A.N., Sosnovskaya, S., Ryumina, E.D., Kharybina, E., Strelkova, O.S., Zhironkina, O.A., Golyshev, S.A., Moiseenko, A., and Kireev, I.I. (2022). Fiber-Like Organization as a Basic Principle for Euchromatin Higher-Order Structure. Front Cell Dev Biol *9*, 784440.

Zurek-Biesiada, D., Szczurek, A.T., Prakash, K., Mohana, G.K., Lee, H.K., Roignant, J.Y., Birk, U.J., Dobrucki, J.W., and Cremer, C. (2016). Localization microscopy of DNA in situ using Vybrant((R)) DyeCycle Violet fluorescent probe: A new approach to study nuclear nanostructure at single molecule resolution. Exp Cell Res *343*, 97-106.